Technical Note

January 21, 2014

π^-/π^+ Separated Response Functions Ratios in Forward Pion Electroproduction on Deuterium at $Q^2 = 0.6 - 2.45$ GeV^2 and $-t = 0.1 - 0.4$ GeV^2

Dr. Cornel Butuceanu and Dr. Garth Huber

University of Regina

Dr. Henk Blok

VU University

Dr. David Gaskell

Jefferson Laboratory

Dr. Tanja Horn

Catholic University of America

Abstract

The study of exclusive $\pi^{\pm}$ electroproduction on the nucleon, including separation of the various structure functions, is of interest for a number of reasons. The ratio $R_L = \sigma_L^{\pi^-}/\sigma_L^{\pi^+}$ is sensitive to isoscalar contamination to the dominant isovector pion exchange amplitude, which is the basis for the determination of the charged pion form factor, $F_\pi(Q^2)$, from electroproduction data. The value of this ratio may also have implications for constraining polarized GPDs with ratios of longitudinal observables. A change in the value of $R_T = \sigma_T^{\pi^-}/\sigma_T^{\pi^+}$ from unity at small $-t$, to a value of 1/4 at large $-t$, would suggest a transition from coupling to a (virtual) pion to coupling to individual quarks. Furthermore, the mentioned ratios may show an earlier approach to pQCD than the individual cross sections. Here, we report on the first complete separation of the four unpolarized electromagnetic structure functions above the dominant resonances in forward, exclusive $\pi^{\pm}$ electroproduction on the nucleon for $Q^2 = 0.6 - 2.45$ $(\mathrm{GeV/c})^2$. The results indicate dominance of the pion-pole diagram at low $-t$.

I. INTRODUCTION

Four amplitudes contribute to pion electroproduction from a nucleon in the one-photon exchange Born approximation model, where a single photon γ^* emitted by the electron couples to the hadronic system: pion-pole, nucleon-pole, crossed nucleon-pole and contact term. The first three amplitudes correspond to Mandelstam t, s and u-channel processes, respectively, Fig. 1. The contact term is used when gauge invariance needs to be restored. Born amplitude based models (1; 2) indicate that for values of the invariant mass W above the resonance region and not too large values of Q^2, the longitudinal part σ_L of the cross section for pion electroproduction at small values of $-t$ is dominated by the t-channel process. The other response functions (transverse σ_T and interference terms σ_{LT} and σ_{TT}) are relatively small. In this regime, the process can be viewed as quasi-elastic scattering of the electron from a virtual pion and thus is sensitive to the pion form factor, F_π. At values of t approaching the pion mass squared (the so called t-pole), the longitudinal response function becomes directly proportional to the charged pion form factor F_π

$$\sigma_L \approx \frac{-tQ^2}{(t-M_\pi^2)^2} g_{\pi NN}^2(t) F_\pi^2(Q^2,t). \tag{1}$$

Here, the factor $g_{\pi NN}(t)$ comes from the πNN vertex and represents the probability amplitude to have a virtual π^+ meson inside the proton at a given t.

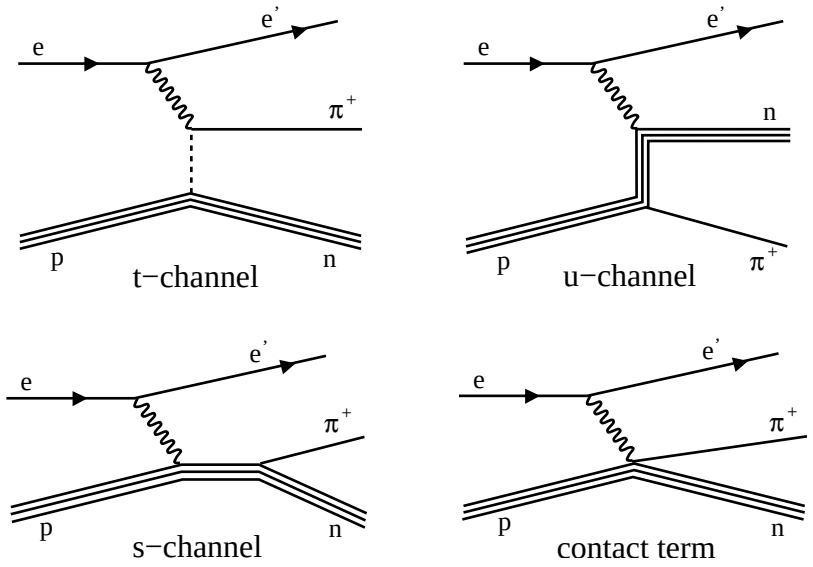

FIG. 1 Born term diagrams for π^+ electroproduction from a proton.

In order to reliably extract F_π, the t-pole process should be dominant in the kinematic region under study. This dominance can be studied experimentally through the ratio of longitudinal

$\gamma_L^* n \to \pi^- p$ and $\gamma_L^* p \to \pi^+ n$ cross sections, which can be expressed in terms of contributions from isoscalar A_S and isovector A_V photon amplitudes:

$$R_L = \frac{\gamma_L^* n \to \pi^- p}{\gamma_L^* p \to \pi^+ n} = \frac{|A_V - A_S|^2}{|A_V + A_S|^2}. \tag{2}$$

As the t-channel process proceeds purely via isovector amplitudes, a deviation of R_L from unity indicates the presence of isoscalar processes. Where the t-pole dominates (small $-t$), the ratio R_L is expected to be close to unity.

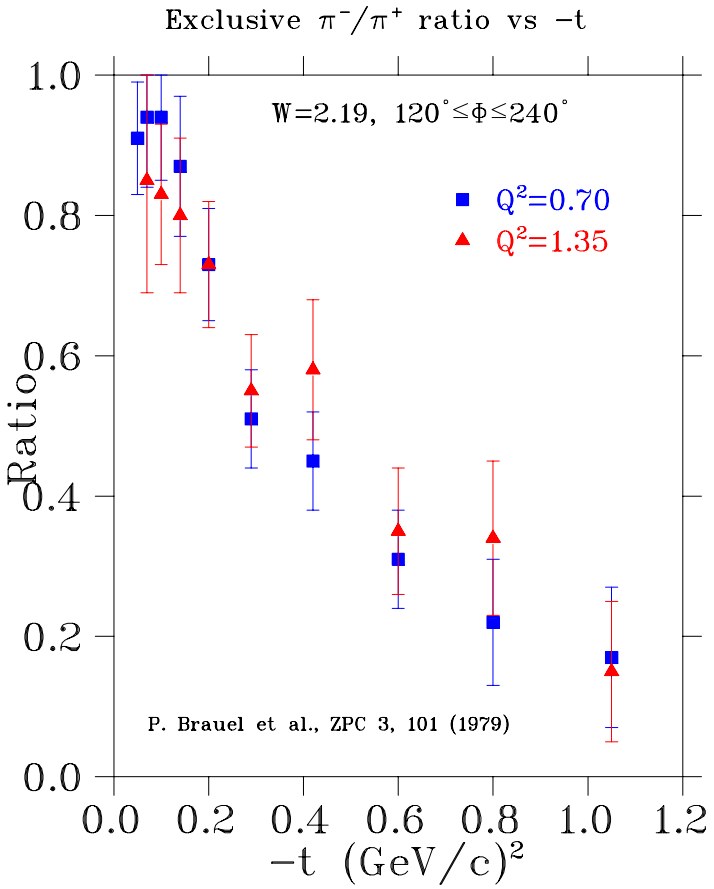

FIG. 2 Exclusive π^-/π^+ upseparated cross section ratio plotted versus $-t$ from Ref. (3). The points depicted by squares represent data taken at $W = 2.19GeV$ and $Q^2 = 0.70$ GeV^2 while the triangles points represent data taken at $W = 2.19GeV$ and $Q^2 = 1.35$ GeV^2.

At low $-t$, also the transverse ratio $R_T = \frac{\gamma_T^* n \to \pi^- p}{\gamma_T^* p \to \pi^+ n}$ is expected to approach unity, because the photon is supposed to couple to the charge of the pion. With increasing $-t$, the photon starts to probe quarks rather than pions. Thus, in the limit of large $-t$, R_T is expected to approach 1/4

given by the square of the ratio of the quark charges involved:

$$R_T = \frac{2Q_d^2}{2Q_u^2} = \frac{(-1/3)^2}{(+2/3)^2} = 1/4 \tag{3}$$

The only previous experimental data on exclusive pion production ratios from deuterium were obtained by P. Brauel *et al.* (3) at DESY. Although these ratios were computed from unseparated cross section data, they support the assumption that at low $-t$ R approaches 1, while at higher $-t$ the data are consistent with 1/4 (see Fig. 2).

We report the results of a new study, where, for the first time ratios of separated response functions (σ_L, σ_T, σ_{LT}, and σ_{TT}) were extracted at several kinematic settings: $Q^2 = 0.6, 1.0, 1.6$ GeV^2 at $W = 1.95$ GeV (F_π-1), and $Q^2 = 2.45$ GeV^2 at $W = 2.22$ GeV (F_π-2), respectively.

II. CORRECTIONS APPLIED TO THE F_π-1 AND F_π-2 DATA SETS

As the experimental technique and analysis of the ^{1}H data acquired in the F_π-1 and F_π-2 experiments have already been presented in detail in Ref. (4), this report will concentrate on those areas where the ^{2}H data and analysis differ from the ^{1}H case.

The settings used in these experiments corresponded to either $^2\mathrm{H}(e,e'\pi^+)nn$ or $^2\mathrm{H}(e,e'\pi^-)pp$ kinematics, where the SOS was always used to detect the scattered electron, and the HMS was used to detect the high momentum π^+ or π^-. These settings are summarized in Table I. As will be discussed in detail, the HMS rates were much higher for the π^- settings than the π^+ settings because of the large electron background at negative spectrometer polarity.

	$^2\mathrm{H}(e,e'\pi^+)nn$	$^2\mathrm{H}(e,e'\pi^-)pp$
Q^2=0.6 GeV^2, W =1.95 GeV (F_π-1)		
ϵ=0.37, E_e =2.445 GeV	3 HMS settings: $\theta_{\pi q}$=+0.5, +2.0, +4.0^o.	2 HMS settings: Missing +2.0^o.
ϵ=0.74, E_e =3.548 GeV	4 HMS settings: $\theta_{\pi q}$=-2.7, +0.0, +2.0, +4.0^o.	1 HMS setting: Only +0.0^o.
Q^2=0.75 GeV^2, W =1.95 GeV (F_π-1)		
ϵ=0.43, E_e =2.673 GeV	2 HMS settings: $\theta_{\pi q}$=+0.0, +4.0^o.	2 HMS settings: $\theta_{\pi q}$=+0.0, +4.0^o.
ϵ=0.70, E_e =3.548 GeV	3 HMS settings: $\theta_{\pi q}$=-4.0, +0.0, +4.0^o.	No data!
Q^2=1.0 GeV^2, W =1.95 GeV (F_π-1)		
ϵ=0.33, E_e =2.673 GeV	2 HMS settings: $\theta_{\pi q}$=+0.0, +4.0^o.	2 HMS settings: $\theta_{\pi q}$=+0.0, +4.0^o.
ϵ=0.65, E_e =3.548 GeV	3 HMS settings: $\theta_{\pi q}$=-4.0, +0.0, +4.0^o.	1 HMS settings: Only +0.0^o.
Q^2=1.6 GeV^2, W =1.95 GeV (F_π-1)		
ϵ=0.27, E_e =3.005 GeV	2 HMS settings: $\theta_{\pi q}$=+0.0, +4.0^o.	Same settings as π^+.
ϵ=0.63, E_e =4.045 GeV	3 HMS settings: $\theta_{\pi q}$=-4.0, +0.0, +4.0^o.	Same settings as π^+.
Q^2=2.45 GeV^2, W =2.2 GeV (F_π-2)		
ϵ=0.27, E_e =4.210 GeV	2 HMS settings: $\theta_{\pi q}$=+1.35, +3.0^o.	Same settings as π^+.
ϵ=0.55, E_e =5.248 GeV	3 HMS settings: $\theta_{\pi q}$=-3.0, +0.0, +3.0^o.	Same settings as π^+.

TABLE I A summary of the ^{2}H kinematic settings taken in the two pion form factor experiments.

A. Event Reconstruction and Tracking

In order to bring the F_π-1 and F_π-2 deuterium experimental data sets to the same level of reconstruction and analysis, the data from the first experiment (two F_π-1 channels: π^- and π^+ electroproduction from deuterium) were replayed using the 2003 analysis engine. It was a considerable effort to adapt the newer engine to accept the format of the older F_π-1 data, which previously had been replayed with the 1998 engine. The reason for this effort is that the 2003 engine incorporates a tracking algorithm with improved multitrack event capabilities, extending the accuracy of the event reconstruction. The details about the new tracking algorithm implemented in the engine are presented in Ref. (5). Because rates in the SOS are low in comparison to the HMS, the discussion of the new algorithm focuses solely upon HMS reconstruction.

Charged particle trajectories are measured by two drift chambers, each with six planes. In the old (1998) Analyzer, the HMS tracking selection criteria was that 4 out 6 planes should have fired in each drift chamber in order to select a "good track", while 5/6 was used for SOS tracking. The new (2003) Analyzer uses the 5/6 method (5 out of 6 planes should have fired in each drift chamber) for both spectrometers, which is much better suited for high rate data (in this case the π^- channel data). The same 5/6 method was used for both the F_π-1 and F_π-2 data sets.

Using matrix elements to describe the transport through the spectrometer, the vertex at the target is then reconstructed from the focal plane coordinates (position; x_{fp} and y_{fp} and direction/slope: x'_{fp} and y'_{fp} of the trajectory at the focal plane). The new tracking algorithm implemented in the engine has several requirements:

- If the program reconstructed only one track, then that track was used.
- If the two or more tracks are reconstructed, then the track that hit the cluster in the calorimeter was used. The calorimeter cut used was quite low so that it was not an effective PID detector, just to get rid of "noise" tracks in the chambers.
- In case two or more tracks hit the cluster in the calorimeter (or neither of them), then in order to select a correct track the following additional criteria were used:
  - If the program reconstructs two or more tracks, then the nearest track to the fired bar in 2Y was chosen.
  - If two or more reconstructed tracks hit the same fired bar in 2Y, then the track nearest to the fired bar in 2X was chosen.
  - If two or more reconstructed tracks hit the same fired bar in 2Y and 2X, then the track with the best χ^2 was chosen (this was the only criteria in the old algorithm).

Use of the new tracking algorithm required several adjustments in the calculation of the tracking efficiency. The tracking efficiency analysis incorporates a cut on good PMT ADC, which excludes events with multiple hits per scintillator plane. In the case where there are multiple tracks in the same scintillator plane, this cut places a bias on the event sample used to calculate the HMS tracking efficiency. Since 2-track events have a lower efficiency than 1-track events, the resulting bias causes the tracking efficiency to be overestimated.

In the case of F_π-2, the requirement of rejecting additional PMT hits outside the fiducial region when calculating the tracking efficiency, which are due mostly to multiple track events, was

removed. The effect of this action was checked using carbon luminosity runs for F_π-2 and the overall results indicated that the high rates up to 1 MHz were understood within 1%, which is a reasonable uncertainty. The overall procedure of extracting the final HMS tracking efficiencies and an additional carbon target check are presented in Section II.C.

B. SOS/HMS Momentum-Angle Correlation Corrections

As discussed in Ref. (6), the iron in the SOS magnets saturates above a certain magnetic field. Below this threshold, field strength the shape of the magnetic field does not change. Beyond this point, the magnetic field shape changes with momentum, and the effective field length decreases. Although the actual field changes are not measured, the effect of these changes upon the particle trajectories are easily observed.

There are two effects, which are corrected for in the reconstruction of the SOS target variables. The first effect is that the normally linear dependence of SOS central momentum upon magnetic field, $p_0 = \Gamma B$, receives an additional B dependence due to a decrease of the SOS effective field length. The central momenta are accordingly corrected, $p_o^{corr} = p_0(1 + \epsilon_p)$. The second effect is that the reconstructed $\delta = (p - p_0)/p_0$ depends on x'_{fp} (when going away from the 1.65 GeV/c setting where the F_π-1 matrix elements were determined). This effect arises from changes in the shape of the fringe fields when saturation sets in, and is corrected for on an event-by-event basis. Both of these corrections are explained in further detail in Ref. (6).

Due to these effects, there is a residual dependence of the reconstructed SOS momentum, δ_{SOS}, upon the reconstructed particle trajectory, x'_{tar}. To account for this, the reconstructed SOS momentum was corrected by adding a central momentum dependent quadratic term, ϵ_δ,

$$\delta_{SOS}^{corr} = \delta_{SOS} + \epsilon_\delta, \tag{4}$$

where the correction is calculated as

$$\epsilon_\delta = (x'_{fp})^2 \left[\sum_{i=0}^{3} a_i p_0^i \right], \tag{5}$$

with x'_{fp} in units of radians, and with $a_0 = 0.47$, $a_1 = -1.37$, $a_2 = 1.81$ and $a_3 = -0.76$ for p_0 above 1 GeV/c. For $p_0 < 1$ GeV/c, the correction used was $\epsilon_\delta = 0.15(x'_{fp})^2$.

For the deuterium data sets studied here, elastic runs on ^{1}H were used to check the validity of these corrections for several momentum ranges. The SOS optics matrix elements used were those extracted from the 1997 (F_π-1) and 2003 (F_π-2) experimental runs. As can be seen from Fig. 3,

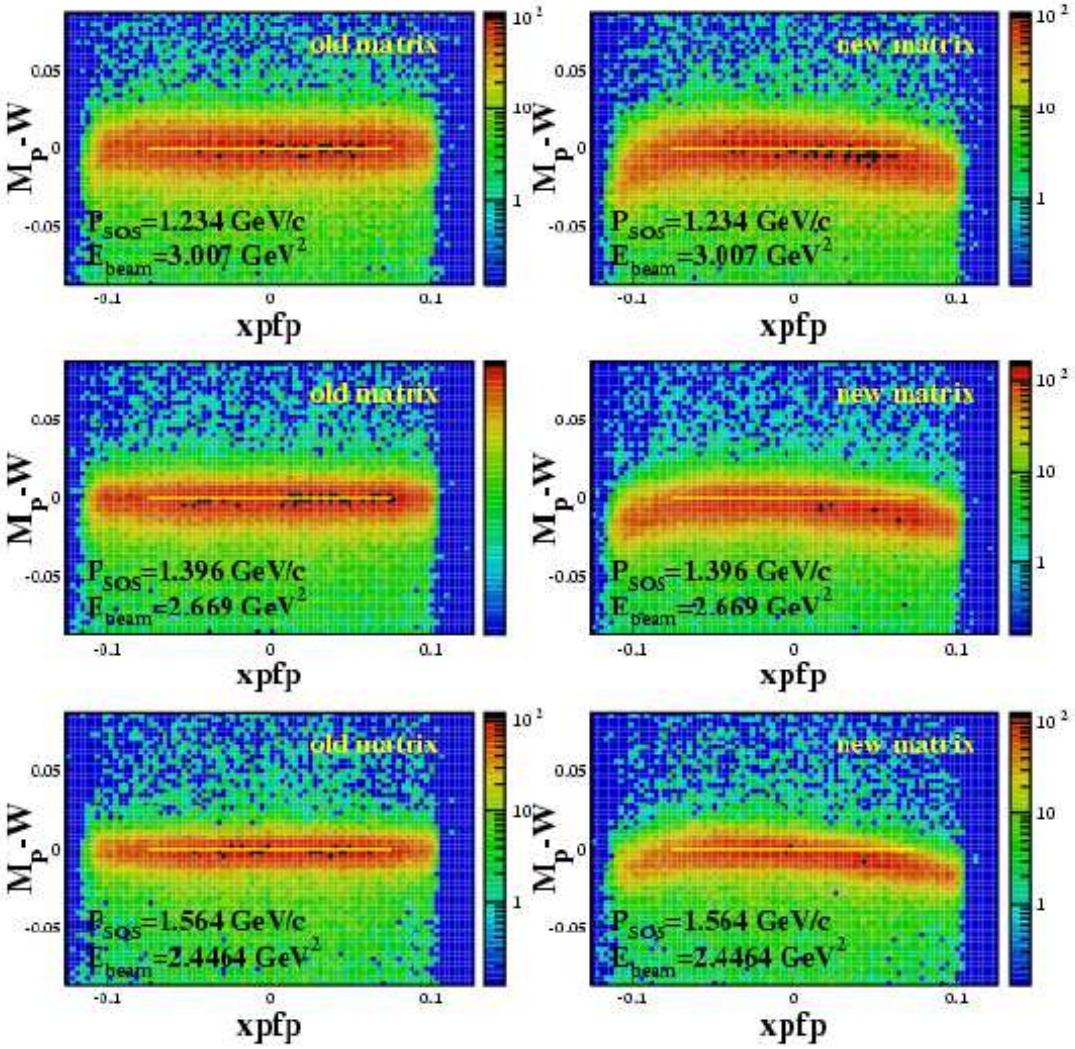

FIG. 3 Proton invariant mass W peak resolution as a function of x'_{fp} for three SOS central momentum settings:1.234 GeV/c (upper panels) and 1.396 GeV/c (middle panels), and 1.564 GeV/c (lower panels) and for SOS Optics Matrix elements extracted from the F_π-1 (left panels) and from the F_π-2 (right panels) elastic data.

for SOS central momenta $p_{SOS} < 1.7$ GeV/c the optics matrix elements extracted from F_π-1 (left panels) elastic data seem to work better than those extracted from the F_π-2 (right panels) elastic data. For central SOS momenta > 1.7 GeV/c, the optics matrix elements extracted from F_π-2 (right panels) work better (Fig. 4). The corrections appropriate to each SOS central momentum range were thus applied to each F_π-1 data set (π^- and π^+). The F_π-2 matrix elements determined in Ref. (7) and discussed in Ref. (8) were used in the analysis of the F_π-2 data, so no further corrections were needed in this case.

A separate correction for the dependence of the HMS momentum on the focal plane trajectory

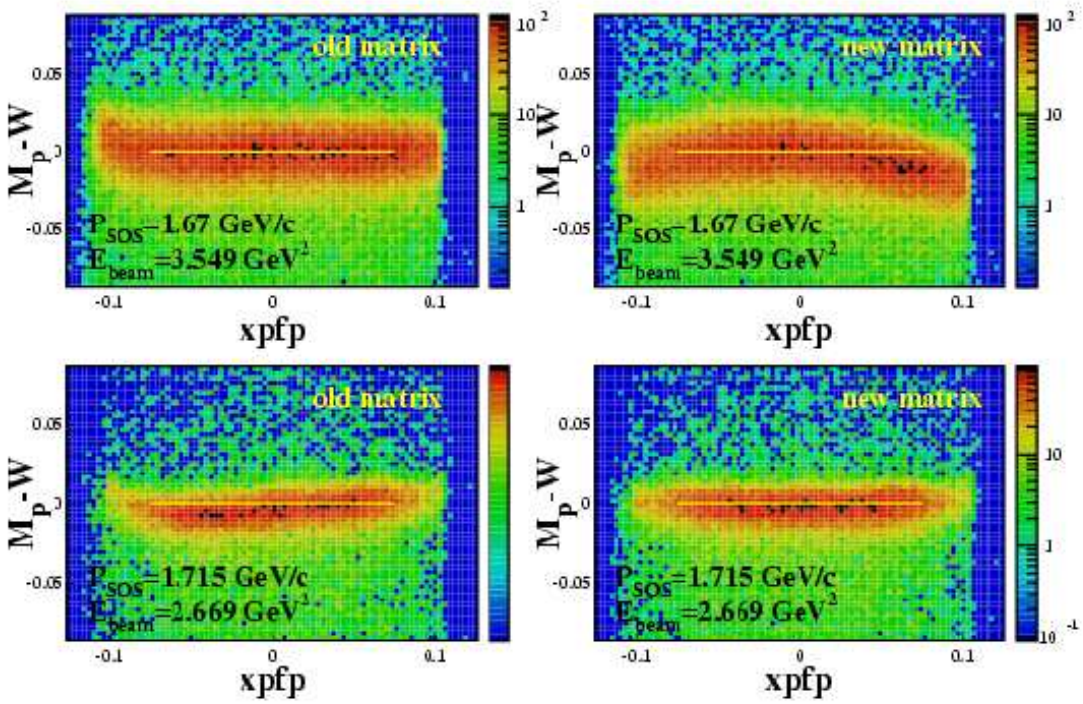

FIG. 4 Proton invariant mass M_p-W peak resolution as a function of x'_{fp} for two SOS central momentum settings:1.67 GeV/c (upper panels) and 1.715 GeV/c (lower panels), and for SOS Optics Matrix elements extracted from the F_π-1 (left panels) and from the F_π-2 (right panels) elastic data.

direction, x'_{fp}, arises because an offset in the Q3 power supply current reading causes a mis-setting of the quadrupole current relative to the tune value. The resulting correlations between the reconstructed HMS momentum, δ_{HMS}, and x'_{fp} were addressed in the same manner as for the SOS. While for the SOS a quadratic form dependent on central momentum was added to δ_{SOS}, for the HMS a simple linear function

$$\delta^{corr}_{HMS} = \delta_{HMS} + c_\delta x'_{fp} \tag{6}$$

sufficed, with c_δ

$$c_\delta = a + b * p_0 HMS, \tag{7}$$

where a=-2.795 and b=-1.280 (Fig. 5). During the F_π-1 experiment, no elastic runs with an electron detected in the HMS were taken, with the exception of few runs taken at the end of the run with $p_{HMS} = 3.67$ GeV/c. For this momentum, the correlation between the invariant mass W and the focal plane trajectory slope x'_{fp}, using two sets of HMS optic matrix elements (1998 and 2003 versions) were used to set the value of the correction factor c_δ for the F_π-1 data, as shown in Figs. 6 and 7.

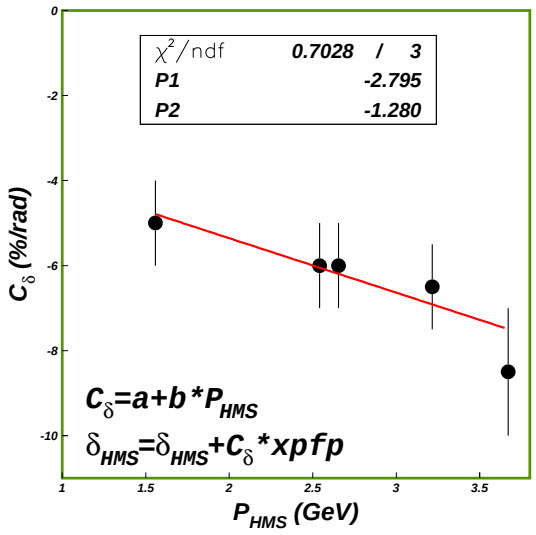

FIG. 5 HMS Q3 correction coefficient (in percent) plotted as a function of HMS elastic electron momentum p_{HMS}.

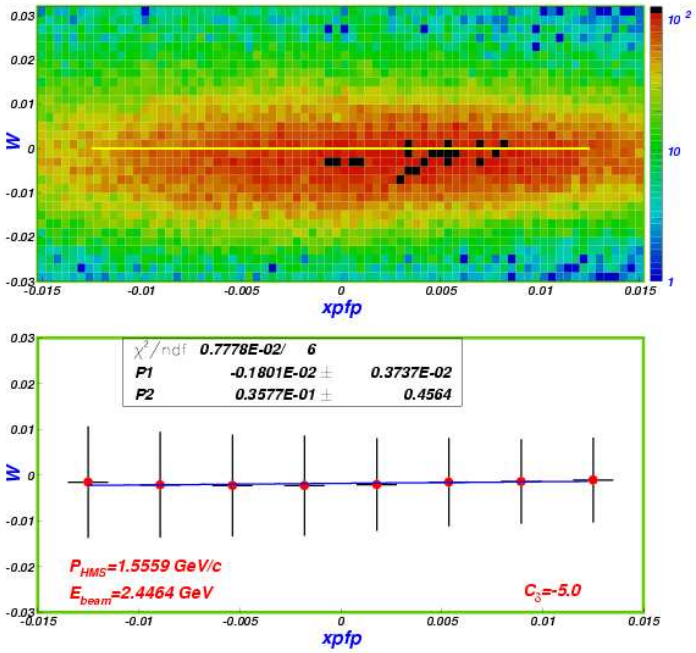

FIG. 6 Proton invariant mass W peak position plotted as a function of x'_{fp} for an HMS delta correction of $c_\delta = 5.0\%$ and for a central HMS momentum of 1.559 GeV/c.

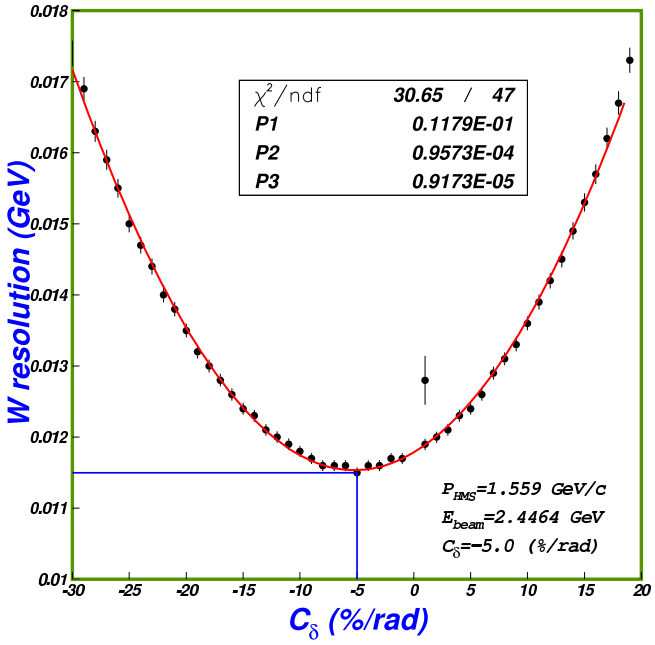

FIG. 7 Proton invariant mass W peak resolution plotted as a function of HMS delta correction c_δ for a central HMS momentum of 1.559 GeV/c.

C. Tracking Efficiencies and Carbon Luminosity Scans

1. Tracking in F_π-1 and F_π-2

The tracking efficiency is defined (8) as the ratio of the number of events for which an actual track is found, to the 'events' that pass through the drift chambers. This ratio is extracted from events in a fiducial area where it is extremely likely that the scintillator hits are due to particles that also traversed the chambers.

The tracking efficiency depends on both the drift chamber hit efficiency and the tracking algorithm used in finding the track. From previous experiments, we know that the efficiency for tracking electrons through the HMS falls linearly with rates, due mainly to the presence of multiple tracks in the drift chambers at high rates. In order to accurately calculate the tracking efficiency, we applied tight particle identification (PID) requirements to select a pure data sample. These requirements are stricter than those used in the regular analysis. In the HMS, the particle identification requirements used to select pions in the tracking efficiency calculation consisted of cuts on the gas Cerenkov and the calorimeter for F_π-1 data, while for F_π-2 an additional cut on the aerogel Cerenkov was applied.

As already mentioned, one of the objectives of this effort was to align both of the F_π-1 and F_π-2 experimental data sets to the same level of reconstruction and analysis. For the first pass reconstruction of the F_π-1 data set, a tracking algorithm was used that did not address multiple track events. Since the π^- data are taken at high rates under the condition of potentially high electron contamination, this deficiency in the tracking algorithm could affect the accurate determination of the π^-/π^+ ratios. Thus, it was decided to reanalyze the F_π-1 data using the new tracking algorithm (5) used for the F_π-2 data set reconstruction. The newly (2003) redesigned tracking algorithm does a significantly better job in selecting the best one of several tracks (multiple tracks) per event than the older version. After adapting the analysis package to accept the format of the older F_π-1 data, the various analysis parameters characteristic to F_π-1 were used in the redesigned reconstruction software, as appropriate.

In the initial tracking efficiency analysis (used in F_π-1), the routine Analyzer/HTRACKING/h_track_tests.f incorporated cuts to exclude multiple good PMT ADC signals within the fiducial region of any hodoscope plane.

The specific lines implementing these cuts are:

```
do i=1,hxloscin(1)-1
if (hscinhit(1,i).EQ.1) hhitsweet1x=-1
```

```
enddo
do i=hxhiscin(1)+1,hscin_1x_nr
if (hscinhit(1,i).EQ.1) hhitsweet1x=-1
enddo

do i=1,hxloscin(2)-1
if (hscinhit(3,i).EQ.1) hhitsweet2x=-1
enddo
do i=hxhiscin(2)+1,hscin_2x_nr
if (hscinhit(3,i).EQ.1) hhitsweet2x=-1
enddo

do i=1,hyloscin(1)-1
if (hscinhit(2,i).EQ.1) hhitsweet1y=-1
enddo
do i=hyhiscin(1)+1,hscin_1y_nr
if (hscinhit(2,i).EQ.1) hhitsweet1y=-1
enddo

do i=1,hyloscin(2)-1
if (hscinhit(4,i).EQ.1) hhitsweet2y=-1
enddo
do i=hyhiscin(2)+1,hscin_2y_nr
if (hscinhit(4,i).EQ.1) hhitsweet2y=-1
enddo

if (abs(sweet1xscin-sweet2xscin).gt.3) hgoodscinhits=0
if (abs(sweet1yscin-sweet2yscin).gt.2) hgoodscinhits=0
```

In the case where there were multiple tracks in the same scintillator plane, these cuts place a bias on the event sample used to calculate the HMS tracking efficiency. Since 2-track events have lower efficiencies than 1-track events, the resulting bias caused the tracking efficiencies to be over estimated. We will call this first method of selecting the data sample the "old" tracking efficiency

method. For the F_π-2 hydrogen analysis, the above lines were commented out, removing the requirement of rejecting additional PMT hits inside the fiducial region and resulting in a "dirty" data sample including multiple-track events. We will call this later method the "new" tracking efficiency method.

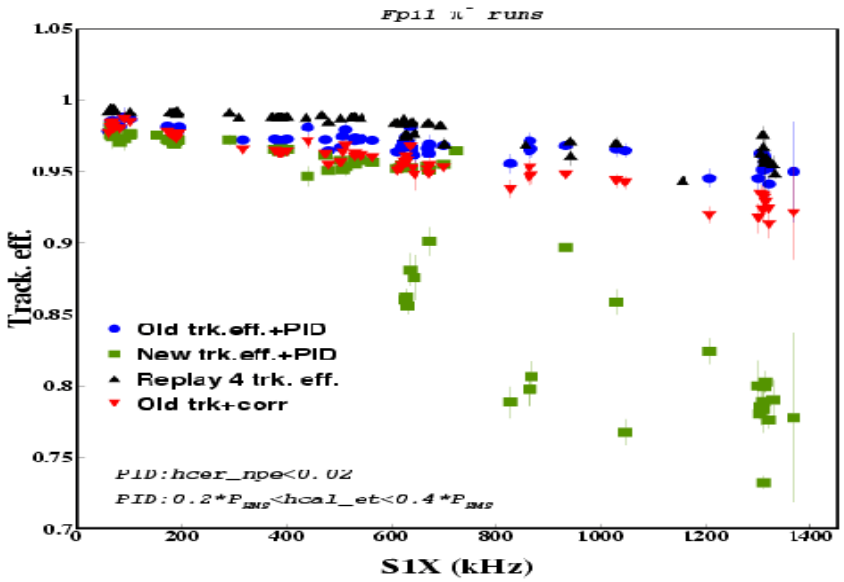

FIG. 8 F_π-1 tracking efficiencies extracted using the "new" (green squares) and "old" (blue dots) methods, plotted as a function of rates. Also shown are the overestimated tracking efficiencies obtained during the first F_π-1 analysis in 1998 (so called "replay 4" in black triangles), and the tracking efficiencies obtained with the "old" method plus a rate dependent correction that accounts for the fact that data for ^{12}C should present no boiling effect (red upside down triangles). Both "replay 4" and "old trk+corr" also include PID.

The "new" tracking efficiency method, with the bias against multiple track events removed, was compared to the "old" tracking efficiency method for both the F_π-1 and F_π-2 π^- deuterium data sets. When making this comparison, it is important to note that the maximum rate encountered in the F_π-1 experiment was 1.3 MHz, while in F_π-2 (benefitting from the operational experience of the first experiment) the maximum rate was limited to 600 kHz. Thus, the F_π-1 deuterium data are much more sensitive to high rate tracking issues than the F_π-2 data.

F_π-1 tracking efficiencies were extracted using the "old" and "new" tracking efficiency methods described above, and they are shown as a function of rates in Fig. 8. The blue dots indicate the tracking efficiencies obtained with the 2003 Engine and the prescription of the "old" tracking efficiency method plus PID cuts, while the green squares indicate the efficiencies obtained with the "new" method plus PID cuts. Also shown (black triangles) are the tracking efficiencies obtained in the last pass of the original F_π-1 analysis using the 1998 Engine, so called "replay 4". Clearly, they were over estimated, as discussed above. The red upside down triangles show the tracking

efficiencies obtained using the "old" method and the 2003 Engine, plus a rate dependent correction, which will be explained later in this section. For the case of the F_π-1 π^- data set, it can be seen (Fig. 8) that the "new" tracking efficiency method compares nicely with the "old" method up to rates $\approx$ 600 kHz, but fails for high rates ($>$ 600 kHz). The "old" method appears to do a fairly good job in describing the expected fall of tracking efficiencies with rates. In contrast, the "new" method is overly sensitive to background hits outside the fiducial region at high rates.

2. F_π-2 Carbon Rate Studies

To obtain a better understanding of the HMS tracking efficiencies, a study of yields from carbon target versus rate and current was performed. In F_π-2, special luminosity scans using different beam currents and different targets (carbon, hydrogen and deuterium) were used to investigate rate and current dependent effects. Due to its very high melting temperature (4554 K), the normalized yields from the carbon target should present no significant current or rate dependence if the various efficiencies are calculated correctly. Unfortunately, no ^{12}C luminosity scans were taken at different beam currents in the F_π-1 experiment, so any conclusions obtained from the F_π-2 study will have to be applied also to the F_π-1 data.

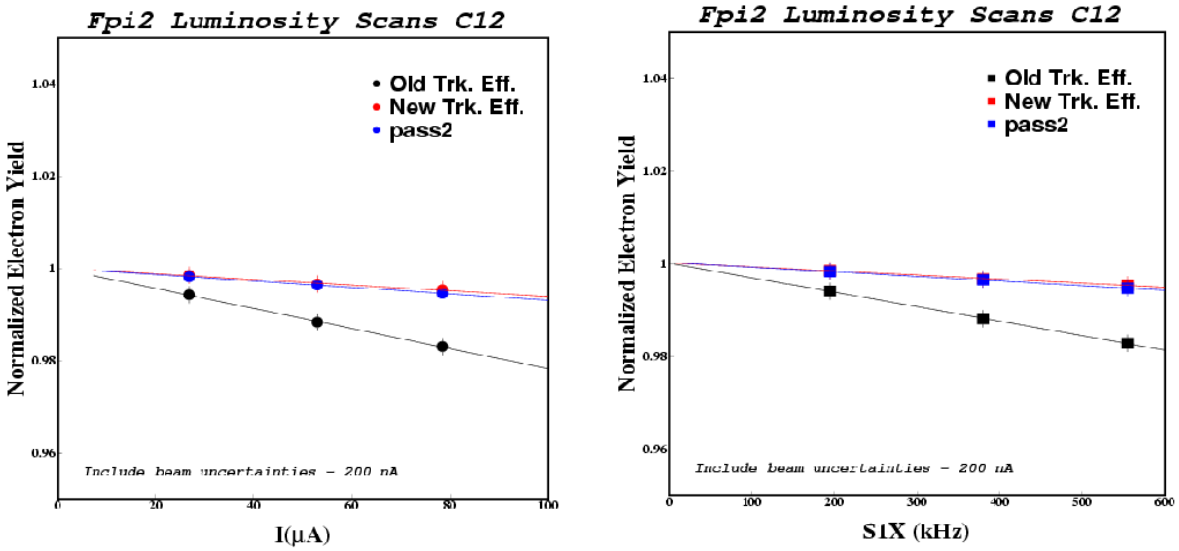

FIG. 9 Normalized $C(e,e')$ yields versus current and rate taken during the F_π-2 experiment. Since carbon targets are insensitive to beam heating effects at high current, the plot of yields versus current should be a horizontal line if all rate dependent effects are correctly taken into account in the data analysis. It is seen that the "new" tracking efficiencies do a better job at high rates than the "old" tracking efficiencies.

For these F_π-2 carbon luminosity scans, we compared the results obtained using the "new" tracking efficiencies to those using a scaler-based analysis, which is independent of the tracking

algorithm. Carbon runs were used to establish if the "new" tracking efficiency would have been consistent with the expected non-boiling effect of a solid target (related to beam current intensity dependence of normalized electron yields). Using tight PID cuts for electrons detected in the HMS, we extracted the normalized yields as a function of beam current, using the form:

$$N_{yields} = \frac{N_e * PS1}{Q_{el} * El_{lt} * CPU_{lt} * Trk_{eff}}, \tag{8}$$

where N_e is the number of electrons obtained using PID cuts, $PS1$ is the prescaling factor applied during the data acquisition, Q_{el} is the accumulated charge, El_{lt} is the electronic live time, CPU_{lt} is the computer live time, and Trk_{eff} is the tracking efficiency obtained using the scaler information and the prescription given by the "old" or "new" methods described earlier. The beam current dependence of normalized yields (including a 200 nA beam current uncertainty due to an offset in the beam current calibration) is shown in Fig. 9.

Fig. 9 indicates that the "new" method of extracting tracking efficiencies (which includes the improved tracking algorithm) is better as far as the F_π-2 carbon luminosity scans are concerned: when the tracking efficiency corrections calculated with the "old" method are inserted into Eqn. 8, a larger boiling effect is observed than when the "new" method efficiencies are used. Since the "old" method for computing the tracking efficiencies is needed for the F_π-1 data set, it is necessary to implement a rate-dependent correction to the "old" method tracking efficiencies. This correction will be applied to both the F_π-1 and F_π-2 data, but is particularly important for the F_π-1 π^- runs, which are at higher rate.

In order to carefully determine this correction, a second study was performed incorporating a greater number of carbon runs taken in two different kinematic settings. Since the probability of a second particle traversing the HMS during the event resolving time is greater at high rates, a tight electron PID cut might introduce its own deadtime not due to tracking efficiency, causing the rate dependence to be underestimated. Therefore, only the following cuts

$$abs(hsdelta) < 8.5 \qquad abs(hsytar) < 5 \qquad abs(hsxptar) < 0.08 \qquad abs(hsyptar) < 0.05 \tag{9}$$

were applied in this study, resulting in the data tabulated in Table II.

Normalized yields from the carbon target were computed using Eqn. 8 and the "old" (htr1) tracking efficiencies in Table II. They are plotted versus rate in Fig. 10. The error bars include statistical uncertainties and an estimated systematic uncertainty of 0.3% added in quadrature, to take into account beam steering on the target and other sensitive effects when no PID cut is applied. Data from the two kinematic settings were separately fit versus rate (blue and red curves

Run	Q_{tot}	hELLO	hS1X	BOT	hS1X/BOT	PS1	htr1	htr2	cpult	hele	SING
$E_e = 4.210$ GeV, $\theta_{HMS} = 12.00$, $P_{HMS} = -3.000$											
47012	100621	181614321	279010493	1106.5	225kHz	697.9	0.9775	0.8781	0.9671	0.9879	168963
47017	44330	80184449	123248274	608.5	203kHz	299.3	0.9794	0.8822	0.9425	0.9903	170741
47018	31249	56737629	87321171	600.5	145kHz	199.7	0.9802	0.8844	0.9394	0.9931	180750
47023	28692	52272441	80556749	923.5	87.2kHz	199.8	0.9827	0.8882	0.9607	0.9959	171278
$E_e = 4.702$ GeV, $\theta_{HMS} = 10.57$, $P_{HMS} = -4.050$											
47757	42974	233316132	303696380	575.5	528kHz	496.4	0.9687	0.9261	0.6415	0.9705	223257
47758	52953	301225113	373411559	660.5	565kHz	992.4	0.9687	0.9242	0.7730	0.9693	165871
47759	124775	675461151	880596706	1590.5	554kHz	1985.1	0.9685	0.9243	0.8738	0.9700	220334
47760	19126	107791771	138777445	710.5	195kHz	249.3	0.9788	0.9059	0.7171	0.9896	233050
47763	56962	308207310	402136284	724.5	555kHz	744.4	0.9690	0.8896	0.7225	0.9699	221788
47764	29473	160260551	209175826	376.5	556kHz	248.2	0.9689	0.9236	0.4685	0.9701	221964

TABLE II HMS carbon luminosity study data taken during F_π-2. No PID cuts are applied. BOT is the average of beam on times 1 & 2 (Threshold cuts: 5 μA for BCM 1 and 1 μA for BCM 2). htr1 is the "old" tracking efficiency (pass 1), while htr2 is the "new" tracking efficiency (pass 2). The final column is the number of HMS singles passing the cuts listed in Eqn. 9.

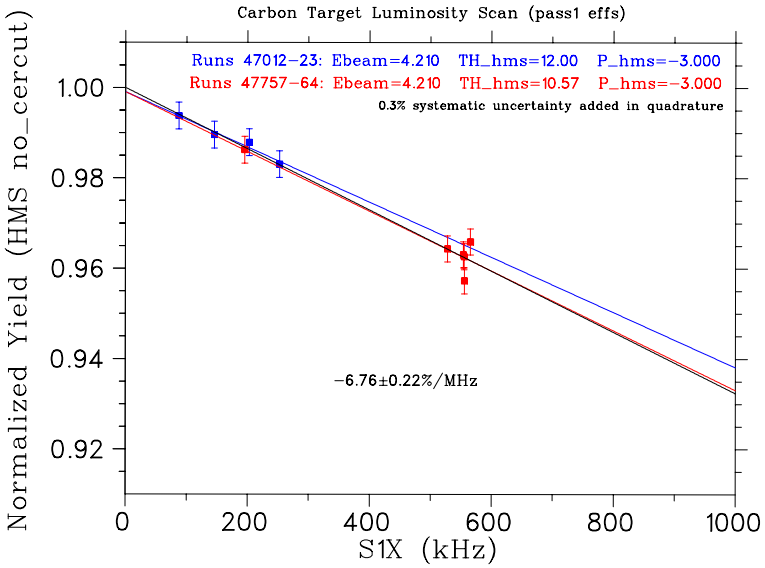

FIG. 10 Normalized yields (no PID cut) from carbon target versus HMS singles rate. The "old" tracking efficiency calculation, using a data sample where multiple track events are rejected, is better suited for higher rates ($>$ 600 kHz). Tracking efficiencies for both of the F_π-1 and F_π-2 data sets were computed using the "old" method and corrected with the linear rate dependent function presented here.

in the figure) and normalized to unity at zero rate. The two data sets, thus normalized, were then fit together, yielding the black curve.

The observed rate dependence suggests that the "old" tracking efficiencies should be corrected in the following manner

$$htr\_corrected = htr\_old \times (1 - S1Xrate(kHz) * 6.76236 \times 10^{-5}). \quad (10)$$

This correction accounts for the difference between the "old" (htr1) and "new" (htr2) efficiencies

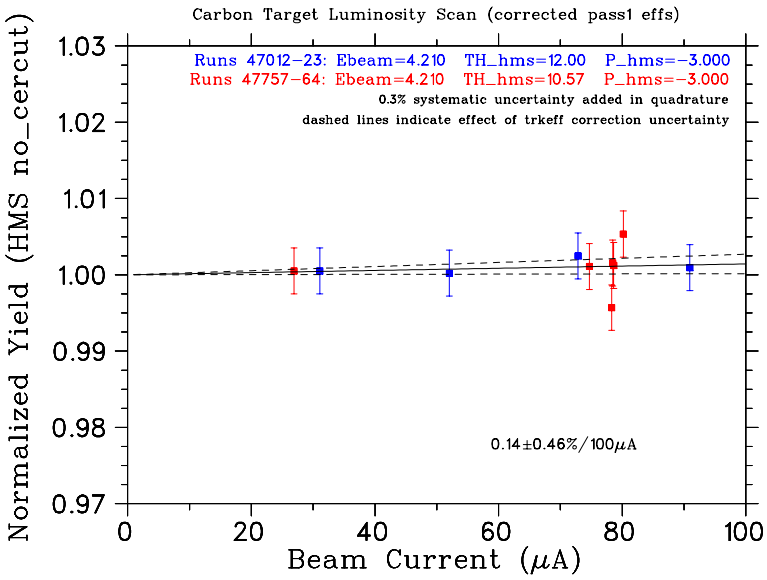

FIG. 11 Carbon yields, after the "old" tracking efficiencies are corrected according to Eqn. 10 versus current, confirming that the applied correction yields consistent results for both kinematic settings. The dashed lines were obtained by applying to the data a tracking efficiency correction raised/lowered by 1σ (Fig. 10), and refitting the current dependence.

in Table II.

Normalized carbon yields, after the "old" tracking efficiencies are corrected according to Eqn. 10, are plotted versus current in Fig. 11. This confirms that the applied correction eliminates spurious rate-dependent effects for both kinematic settings, even though they are taken at significantly different combinations of rates and currents.

To summarize, the old tracking efficiencies plotted in Fig. 8 were corrected for the tracking efficiency dependence upon rate shown in Fig. 10 and applied to the normalized pion yields (for both F_π-1 and F_π-2).

The systematic uncertainties in the HMS tracking efficiencies were estimated as follows. In the F_π-2 hydrogen analysis, the tracking efficiencies were assigned a 1.0% scale and an 0.4% ϵ-uncorrelated systematic uncertainty (4; 8), where the first is the scale uncertainty primarily at low rate and the second is due to a variety of factors which may affect high and low ϵ settings differently, such as the greater scatter exhibited by tracking efficiencies at high rates. The same effect is seen in Fig. 8, where the F_π-1 π^- "old" tracking efficiencies have an increased scatter of approximately $\pm 1.25\%$ at 1.3 MHz. There is an additional uncertainty of 0.2%/MHz due to the tracking efficiency correction discussed above. Since the maximum rate variation for the F_π-1 π^+ settings, and for all F_π-2 $\pi^\pm$ settings, is about 400 kHz, this gives an ϵ-uncorrelated systematic uncertainty of 0.45%. However, the F_π-1 π^- settings have a maximum rate variation of 1.2 MHz,

corresponding to an ϵ-uncorrelated systematic uncertainty of 1.3%.

D. Cryotarget Boiling Correction

When the electron beam hits the liquid target, it produces a large power deposition per unit target area and as a result induces localized density fluctuations referred to as "target boiling". In order to reduce these fluctuations, the beam was rastered over a small area rather than localizing it at one point on the target. The target boiling effect can be measured by comparing the yields at fixed kinematics and varying beam current. During both experiments (F_π-1 and F_π-2), dedicated luminosity elastic runs were taken for both liquid targets (Hydrogen and Deuterium). The two experiments used cryotargets with significantly different geometries, as well as significantly different beam raster patterns, leading to very different boiling effects.

Run	Q_{tot}	hELLO	hS1X	BOT	PS1	htr1	htr2	cpult	hele	S1.5	S2	S99
Q^2=2.45, low ϵ, $E_e = 4.21$ GeV, $\theta_{HMS} = 10.54$												
47190	35632	593645749	759588827	1032.5	1978.1	0.9658	0.8383	0.9047	0.9589	2834	2999	150861
47191	21863	370444977	477096355	1115.5	596.3	0.9734	0.8528	0.9170	0.9765	6577	6926	327205
47192	10301	176604087	228444444	1089.5	299.1	0.9790	0.8636	0.9347	0.9886	6620	6990	323435
47241	27317	454374146	581377706	809.5	989.2	0.9656	0.8351	0.8788	0.9592	4215	4478	225052
47242	17066	284001092	363506739	530.5	989.4	0.9656	0.8372	0.8800	0.9600	2633	2768	141946
47243	15933	269682797	347254506	828.5	298.2	0.9732	0.8518	0.8671	0.9769	8872	9435	451950
47244	12196	206390831	265833195	632.5	298.2	0.9734	0.8526	0.8671	0.9768	6898	7294	346316
47245	6118	104824677	135564178	661.5	99.7	0.9792	0.8633	0.8435	0.9890	10561	11098	521854
47246	5437	93131752	120435159	578.5	99.7	0.9790	0.8621	0.8403	0.9888	9214	9722	460107
Q^2=2.45, low ϵ, $E_e = 4.21$ GeV, $\theta_{HMS} = 12.21$												
47266	56228	431953502	559403421	1134.5	992.9	0.9718	0.8599	0.9006	0.9734	4611	4876	234392
47267	32848	255082402	331707652	1114.5	398.3	0.9766	0.8704	0.9163	0.9840	7211	7597	357745
47296	10513	82800190	108090906	1132.5	99.9	0.9824	0.8809	0.9234	0.9950	9913	10298	475933
47297	49966	383049896	494990723	921.5	991.4	0.9697	0.8552	0.8743	0.9689	3976	4195	201027
Q^2=2.45, high ϵ, $E_e = 5.25$ GeV, $\theta_{HMS} = 10.61$												
47480	9204	65677147	106143067	955.8	149.8	0.9802	0.8615	0.8848	0.9945	37161	37467	256839
47481	3327	23751902	38382157	349.0	99.8	0.9802	0.8598	0.8425	0.9945	19019	19187	132571
47483	38898	272602333	435706188	806.5	992.1	0.9697	0.8397	0.7671	0.9723	18521	18793	133363
Q^2=2.45, high ϵ, $E_e = 5.25$ GeV, $\theta_{HMS} = 16.61$												
47510	65033	48592122	139812146	912.5	59.9	0.9784	0.8785	0.7819	0.9958	54175	54716	442817
47511	14012	10469724	30143430	194.5	59.9	0.9751	0.8746	0.7815	0.9958	11706	11820	95212

TABLE III Singles data taken with SCIN-3/4 HMS trigger during F_π-2 π^- running. No PID cuts are applied. BOT is the average of beam on times 1 & 2 (Threshold cuts: 5 μA for BCM 1 and 1 μA for BCM 2). htr1 is the "old" tracking efficiency (pass1), while htr2 is the "new" tracking efficiency (pass2). The final column (S99) is the number of HMS singles events passing the cuts listed in Eqn. 11, while S1.5 and S2 have in addition cuts of $hcer\_npe < 1.5$ and $hcer\_npe < 2$ applied.

F_π-2 used the "tuna can" cryotarget geometry [1] and circular beam raster design, which are

[1] Cylindrical cryotarget with its axis vertical, transverse to the beam.

expected to result in boiling corrections $< 1\%$ (8). However, that determination was done using the "new" tracking efficiencies. To ensure that the appropriate correction is applied when "corrected old" tracking efficiencies are used, this study was repeated, using ^{2}H negative polarity HMS data taken with a SCIN-3/4 trigger. Dedicated runs with a wide variety of electron beam currents were taken for all π^- kinematic settings except Q^2=2.45, high ϵ, $E_e = 5.25$ GeV, $\theta_{HMS} = 13.61$.

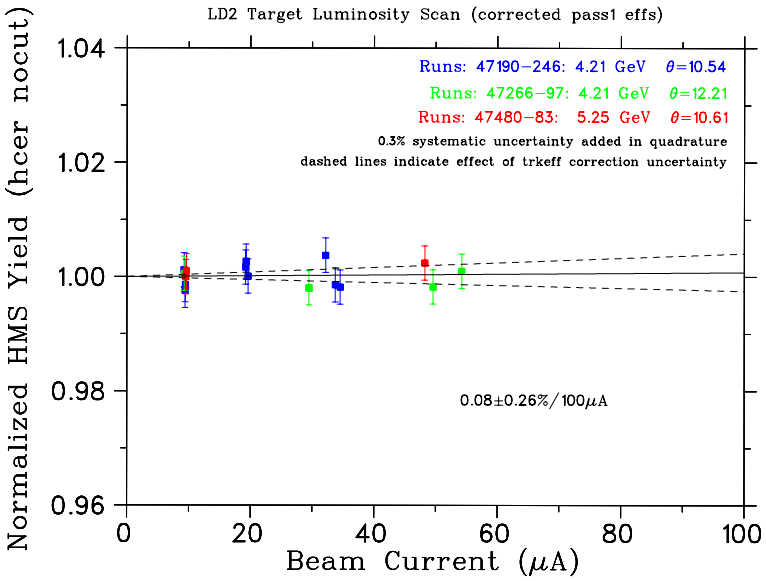

FIG. 12 Normalized HMS singles yields from F$_\pi$-2 ^{2}H π^- production data taken with a SCIN-3/4 trigger, plotted as a function of beam current. The dashed lines were obtained by applying to the data a tracking efficiency correction raised/lowered by 1σ (Fig. 10), and refitting the current dependence.

Cuts of

$$abs(hsdelta) < 8.0 \qquad abs(hsxptar) < 0.09 \qquad abs(hsyptar) < 0.055 \tag{11}$$

were applied to ntuples from each of these runs, resulting in the data tabulated in Table III. The "old" tracking efficiencies (htr1 in the table) were corrected via Eqn. 10. The normalized pion yield was calculated for each run according to

$$N_{yields} = \frac{N_{sing} * PS1 + N_{coin}}{Q_{el} * El_{dt} * CPU_{dt} * Trk_{eff}}. \tag{12}$$

N_{sing} is the column labeled S99 (no Cerenkov cut) in the table. N_{coin} is the corresponding number of coincidences obtained by the same analysis, corrected for the SOS electronic live time. [For brevity, the coincidence data (C99) is not listed in the table.]

The normalized yields are plotted versus current in Fig. 12. The error bars include statistical uncertainties and an estimated systematic uncertainty of 0.3% added in quadrature. Data from

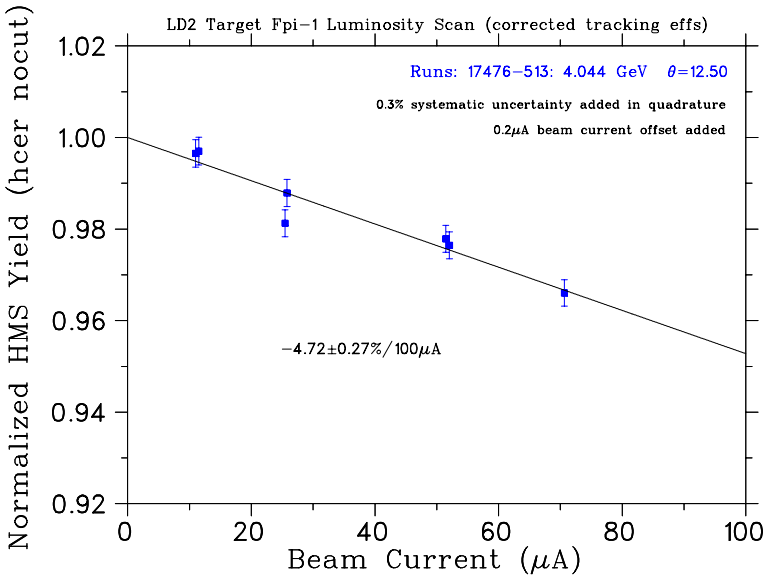

FIG. 13 Normalized HMS yields from F_π-1 ^{2}H elastics data taken with electron trigger plotted as a function of beam current. A $+0.2\mu$A beam current offset is applied, as described in the text.

the three kinematic settings were separately fit versus current and normalized to unity at zero current. The three data sets, thus normalized, were then fit together, yielding the black curve. The observed current dependence suggests that no correction should be applied, which is similar to the conclusion reached in Ref. (8), where a $<1\%/100\mu$A correction was determined using the "new" tracking efficiencies.

Run	Q_{tot}	hS1X	BOT	PS1	htr	cpult	hele	SING
$E_e = 4.044$ GeV, $\theta_{HMS} = 12.50$, $P_{HMS} = -3.670$								
17476	4381	39912098	387.5	50	0.9816	0.5432	0.9983	241548
17481	7346	67005769	680.1	50	0.9818	0.5551	0.9984	414269
17487	6182	54761791	241.6	200	0.9763	0.6877	0.9964	104189
17488	23038	198857869	912.3	200	0.9762	0.6905	0.9963	387456
17491	69286	594124739	1351.4	500	0.9658	0.7335	0.9934	477416
17511	40311	345624687	777.5	300	0.9662	0.6196	0.9937	390612
17513	73205	613217684	1039.2	600	0.9569	0.6792	0.9913	375792

TABLE IV HMS elastics luminosity study data taken during F_π-1. No PID cuts are applied. htr is the "old" tracking efficiency, which is subsequently corrected by Eqn. 10. The final column is the number of HMS singles events passing the cuts listed in Eqn. 9.

F_π-1 used the so-called "soda can" cryotarget geometry [2] and "bed post" beam rastering [3], which leads to a significant boiling correction. The magnitude of this correction is sensitive to the rate-dependent correction applied to the HMS tracking efficiencies. The cuts listed in Eqn. 9 were

[2] Cylindrical cryotarget with its axis horizontal, in the direction of the beam.
[3] See Fig 3.3 of Ref. (6)

applied to ntuples from luminosity-study runs, resulting in the data tabulated in Table IV. The "old" tracking efficiencies were corrected via Eqn. 10 and normalized yields calculated according to Eqn. 8. In analyzing these data, it was found that the slope of yield versus beam current was overly sensitive to the inclusion of the lowest current points in the fit. A significantly reduced sensitivity to these points was obtained with the addition of a $+0.2\mu$A beam current offset, which was subsequently applied in all F_π-1 yield calculations. A similar current offset was used in Ref. (9).

The corrected data were thus fit versus current and normalized to unity at zero current, yielding the black curve in Fig. 13, and a ^{2}H target density correction of $(4.72 \pm 0.27\%)/100\mu$A. The error bars include statistical uncertainties and an estimated systematic uncertainty of 0.3% added in quadrature. The resulting cryotarget boiling correction is larger than the $(1.15 \pm 0.31\%)/100\mu$A correction determined for a nearly identical ^{2}H cell in Ref. (9), but is similar to the $(6\pm1\%)/100\mu$A correction determined for the F_π-1 ^{1}H cell in Ref. (6).

E. HMS Cerenkov Blocking Correction

The HMS threshold gas Cerenkov detector is used to ensure good e^-/π^- separation. In both F_π-1 and F_π-2, the HMS gas Cerenkov detector was used as a veto in the trigger for π^- runs to avoid high DAQ deadtime due to large e^- rates in the HMS. The effective gas Cerenkov thresholds used in the hardware veto are similar for both experiments. Since the actual veto threshold varies slightly from run to run due to PMT gain variations at high rates, slightly more restrictive software thresholds of 1.5-2 photoelectrons were applied in the data analysis. Additionally in the F_π-2 experiment, an Aerogel Cerenkov detector was used for separating protons and π^+ for central momenta above 3 GeV/c.

There is a loss of pions due to electrons passing through the gas Cerenkov within ≈ 100 ns after a pion has traversed the detector, resulting in a mis-identification of the pion event as an electron and being eliminated by the analysis cuts applied (Cerenkov blocking). A correct estimation of the Cerenkov blocking correction is essential in extracting the π^- cross section and is implicit in the final estimation of π^-/π^+ ratios of separated response functions. A variety of studies were performed to determine the corrections that should be applied to both experiments.

1. F_π-2 TDC Studies

Fig. 14 shows multi-hit TDC spectra of the Cerenkov signal into the HMS trigger for two π^- SCIN-3/4 runs (i.e. no Cerenkov veto). The TDC is started by the HMS pretrigger signal and can be stopped multiple times by the retimed (i.e. delayed and discriminated) Cerenkov signal. The main peak corresponds to signals (primarily electrons) that result in the trigger, starting the TDC. Events not associated with the original trigger (other electrons or pions) appear as additional events to the left and right of the main electron peak. The second peak to the right is due to a second electron arriving within the timing window, but after the discriminator "dead window" of ∼40 ns (caused by the length of the discriminator pulse). The backgrounds to the left and right of the two peaks are due to earlier and later electrons, while the tail extending to 410 ns is due to pedestal noise that crosses the discriminator threshold. The peak at channel 4096 is the accumulation of very late TDC stops, while zeros correspond to electrons (or pions) that did not give a stop.

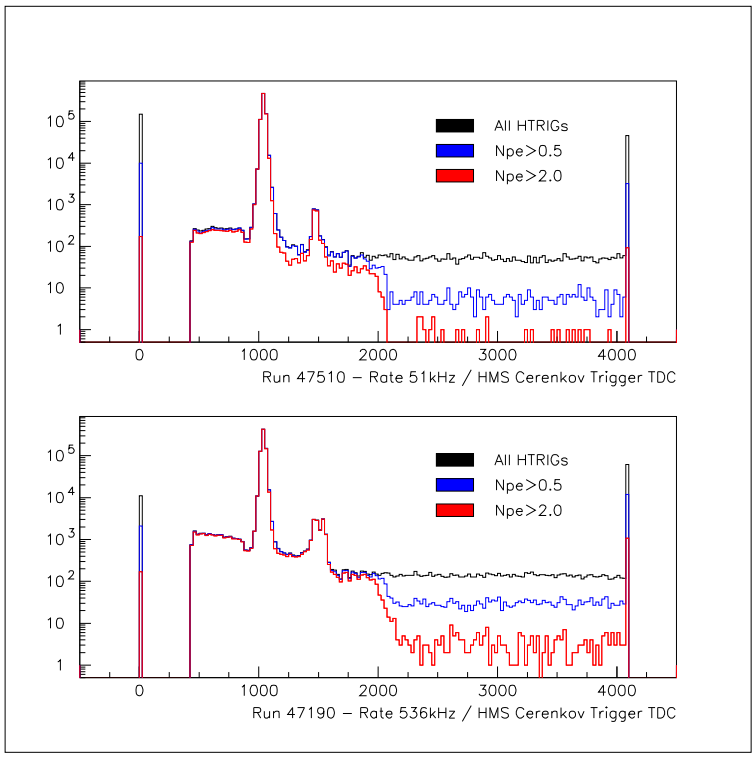

FIG. 14 TDC spectra of the Cerenkov signal into the HMS trigger for two π^- runs where the HMS trigger was SCIN-3/4. A series of cuts are placed on the number of Cerenkov photoelectrons to select "electron" events. The hornizontal scale is TDC channels, where the TDC scale is 100 ps/chan.

The features of the TDC spectra were investigated for a variety of SCIN-3/4 π^- runs, for HMS singles rates up to ∼600 kHz. As indicated by the differences between the low rate and high rate runs plotted in Fig. 14, the main peak to pedestal ratio degrades with increasing rate, and the

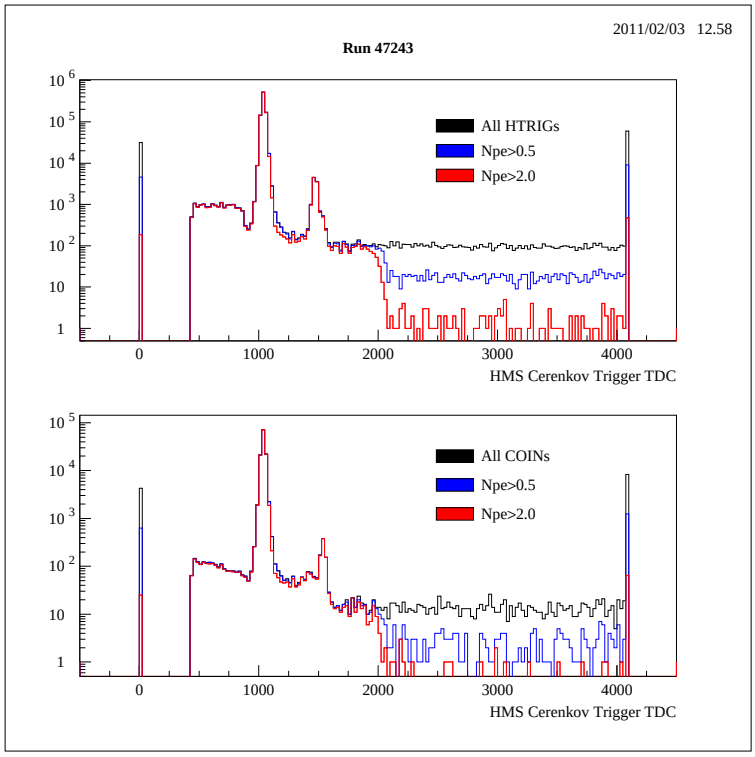

FIG. 15 Cerenkov trigger TDC for π^- run 47243, where the HMS trigger was SCIN-3/4. The mean HMS rate for this run, as computed from the ELLO scaler is 325 kHz. The top panel is the TDC spectrum for HMS singles events, while the bottom panel is for coincidence events. The TDC scale is 100 ps/chan.

second peak to first peak ratio gets larger. The growth of the second peak relative to the first peak was confirmed to have a $\tau = 37 \pm 1$ns time constant, which is consistent with the expected TDC deadtime due to the TDC stop gate width as indicated by the spacing between the main and second peaks.

We also confirmed that the basic features of the TDC spectra are the same for HMS singles and HMS+SOS coincidences. Fig. 15 shows this for a representative run. While the structure of the second peak is a bit different for reasons which we do not completely understand, the pedestal width and peak locations are the same in both cases. This lends confidence that any Cerenkov blocking correction determined from HMS singles data (due to smaller statistical uncertainties) should be applicable to the coincidence data as well.

While the events to the left of the 'notch' next to the main peak correspond to early electrons passing through the detector before the electrons associated with the trigger (which are already addressed in the coincidence time blocking correction), events to the right of the main peak correspond to electrons traversing the detector after the original trigger electrons, and the pedestal underneath the main peak is due to concurrent electrons within the TDC deadtime. The concur-

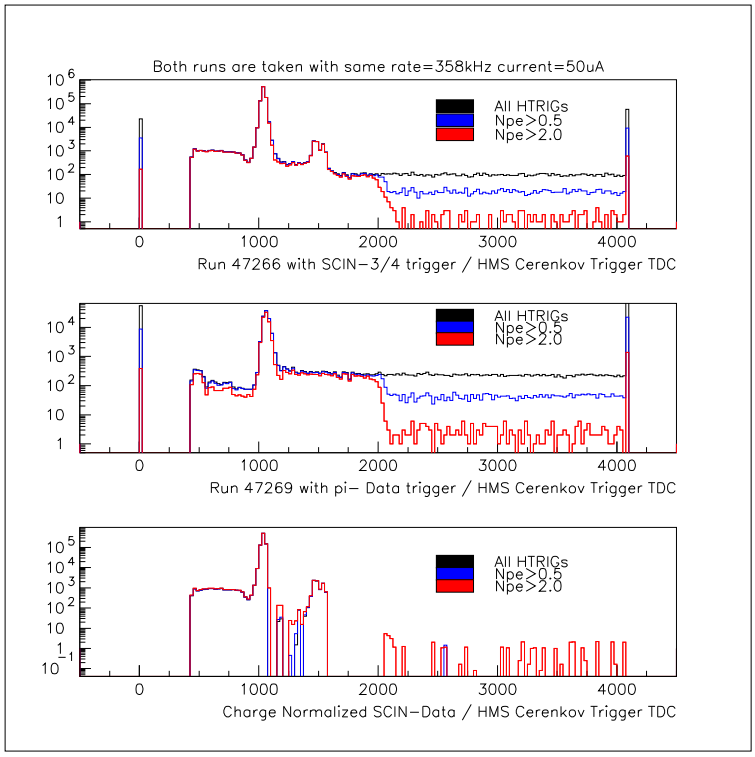

FIG. 16 Cerenkov trigger TDC for two π^- runs taken under identical beam current and singles rate conditions, but different HMS trigger conditions. The only other differences between these runs are the singles prescale factor and the CPU livetime. The bottom panel is their difference, where the data run has been normalized by charge, cpult and PS1 to the SCIN-3/4 run and then subtracted. The TDC scale is 100 ps/chan.

rent and later events contribute to Cerenkov blocking and must be corrected for. The time from the notch to the left of the main peak (Chan 900) to the edge of the plateau (Chan 2050) indicates an effective Cerenkov TDC gate width of 116.4 ± 6.3 ns, where the uncertainty is estimated from the slope of the right falling edge and the width of the notch.

Five pairs of π^- runs were identified where for each pair the beam and rate conditions were identical, but the HMS trigger conditions were different (see Table V). The TDC spectra for one of these pairs is shown in Fig. 16. While one should expect the second peak to be much smaller in the π^- data run than in the SCIN-3/4 run, we are a bit surprised that it is completely absent in the data run. Perhaps the lack of a TDC deadtime effect when the first electron is vetoed causes later electron stops to be spread further to the right, instead of piled up in a second peak. The regular π^- data run (middle panel) also exhibits some structure to the left of the main peak but otherwise the features are consistent with our expectations. The ratio of zeros to main peak counts is much greater in the π^- data run, which is consistent with the zeros being primarily pions and the main peak being electrons. The normalized difference of the two runs (bottom panel) indicates that the Cerenkov trigger is about 90% efficient at vetoing electrons.

Run	Q_{tot}	hELLO	hS1X	BOT	PS1	htr1	htr2	cpult	hele	S1.5	S2	C1.5	C2
Q^2=2.45, low ϵ, $E_e = 4.21$ GeV, $\theta_{HMS} = 10.54$													
47190	356312	593645749	759588827	1032.5	1978.1	0.9311	0.3590	0.9047	0.9589	2046	2071	3894	3941
47193	117729	1951678625	2497749072	3400.5	2994.4	0.9299	0.3585	0.9851	0.9941	4899	4963	13964	14194
Q^2=2.45, low ϵ, $E_e = 4.21$ GeV, $\theta_{HMS} = 12.21$													
47266	56228	431953502	559403421	1134.5	992.9	0.9286	0.4008	0.9006	0.9734	3314	3335	4227	4264
47269	169246	1301200129	1684928207	3587.5	2996.1	0.9324	0.4043	0.9874	0.9965	3687	3720	14577	14746
Q^2=2.45, low ϵ, $E_e = 4.21$ GeV, $\theta_{HMS} = 12.21$													
47297	49966	383049896	494990723	921.5	991.4	0.9326	0.4078	0.8743	0.9689	3070	3094	4600	4731
47298	166228	1274314538	1646468086	2986.5	3993.8	0.9333	0.4032	0.9840	0.9958	2776	2799	16838	17017
Q^2=2.45, high ϵ, $E_e = 5.25$ GeV, $\theta_{HMS} = 10.61$													
47483	38898	272602333	435706188	806.5	992.1	0.9667	0.7294	0.7671	0.9723	16075	16188	37391	37645
47477	137020	959986136	1533128246	2872.5	5785.6	0.9657	0.7271	0.9397	0.9927	11619	11704	156783	158043
Q^2=2.45, high ϵ, $E_e = 5.25$ GeV, $\theta_{HMS} = 16.61$													
47510	65033	48592122	139812146	912.5	59.9	0.9641	0.7608	0.7819	0.9958	46298	46446	10983	11020
47514	251361	186978517	531086990	3510.5	699.0	0.9642	0.7672	0.9766	0.9990	18820	18879	52502	52663

TABLE V Selected F_π-2 π^- runs taken under identical beam and rate conditions, except that the HMS trigger conditions are different. The first run of each pair is a Cerenkov veto Test Run with SCIN-3/4 HMS trigger, and the second is a regular π^- Data Run. The column quantities are as in Table III, except that C1.5, C2 indicate coincidence events with $hcer\_npe < 1.5$ and $hcer\_npe < 2$ cuts applied.

2. F_π-2 Singles Yield Study

The same comparison of runs with same rate but different trigger condition can also be used to determine the effective threshold of the Cerenkov trigger veto. The sample comparison shown in Fig. 17 indicates an effective veto threshold of approximately 2.5 npe. However, please note that this comparison suffers from normalization uncertainties due to deadtime effects – a plain subtraction of the Cerenkov trigger veto run from the scintillator run gives negative counts at low npe, as noted in the caption. Because PMT gain variations and pile-up effects will cause the actual veto threshold to vary with rate, a slightly more restrictive software threshold of $hcer_{npe} < 2.0$ was uniformly applied in the F_π-2 data analysis to cut out electrons.

As already discussed in Sec. II.D, dedicated runs were taken with SCIN-3/4 trigger for a variety of electron beam currents for all F_π-2 π^- kinematic settings except Q^2=2.45, high ϵ, $E_e = 5.25$ GeV, $\theta_{HMS} = 13.61$. The purpose of these runs was to determine the Cerenkov blocking correction versus electron rate into the HMS. The data with $hcer_{npe} < 2.0$ software threshold listed in Table III were used to compute normalized pion yields in a manner similar to Eqn. 12, except that the tracking efficiency correction Eqn. 11 was applied. [Note that it might have been better to use the ELCLEAN rate in this study, however, the object is to obtain a correction which can be applied to both experiments and ELLO is the closest equivalent scaler available in F_π-1.]

To determine whether the yields for the different sets of kinematics exhibit similar rate depen-

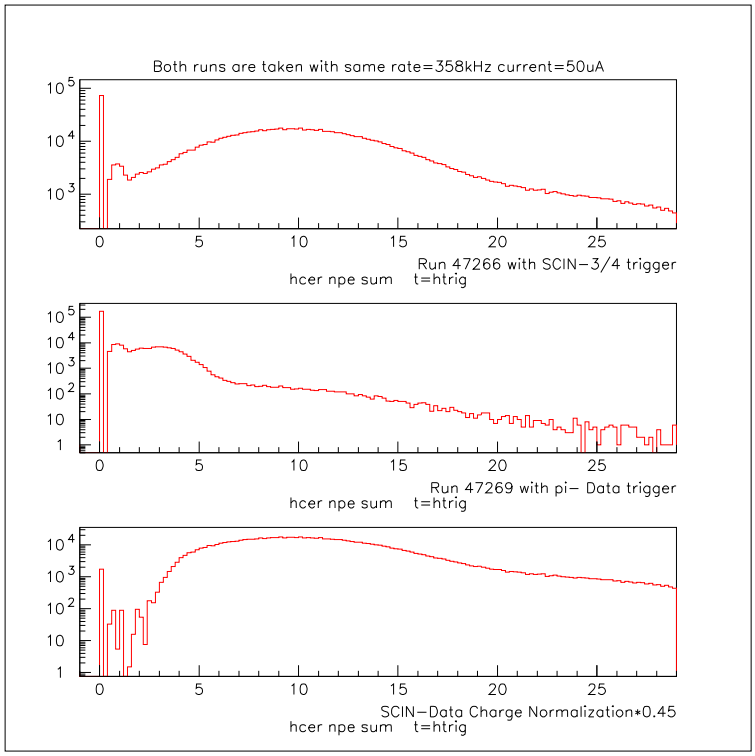

FIG. 17 Cerenkov photoelectron spectra for two π^- runs taken under identical beam current and singles rate conditions, but different HMS trigger conditions. The bottom panel is their charge normalized difference, where the normalization factor has been multiplied by 0.45 to avoid negative counts at low npe.

dencies, the first three sets in Table III, which span a large range of rates, were fit to functions of the form $Y = A^{-R\tau}$, where both A and τ were free parameters. Although A introduces an additional free parameter to the fit, this allows τ to be extracted for each set without being sensitive to the normalization of the 'low rate yield'. The normalized yields versus rate, and the fit τ values are shown in Fig. 18. The obtained effective gate widths are reasonably independent of kinematic setting. Because the runs at Q^2=2.45, high ϵ, $E_e = 5.25$ GeV, $\theta_{HMS} = 16.61$ are only at low rates, that that τ value is not shown.

Two of the three shown τ_{eff} values have nearly the same values, while the third is 1.5σ larger. Additional studies were performed to see if the larger τ value could be due to a different π/e ratio at this setting compared to the others. The π/e ratio was found to depend upon incident beam energy, and was nearly insensitive to spectrometer rate and angle, so it could not be the cause of the discrepancy. We conclude the three τ values are consistent within normal statistical fluctuation, and that other factors that could affect the conclusions are reasonably well under control. Since they are consistent, a combined fit of all the data was made. The three data sets were independently normalized to unity at zero rate, effectively removing the cross section variation with kinematics.

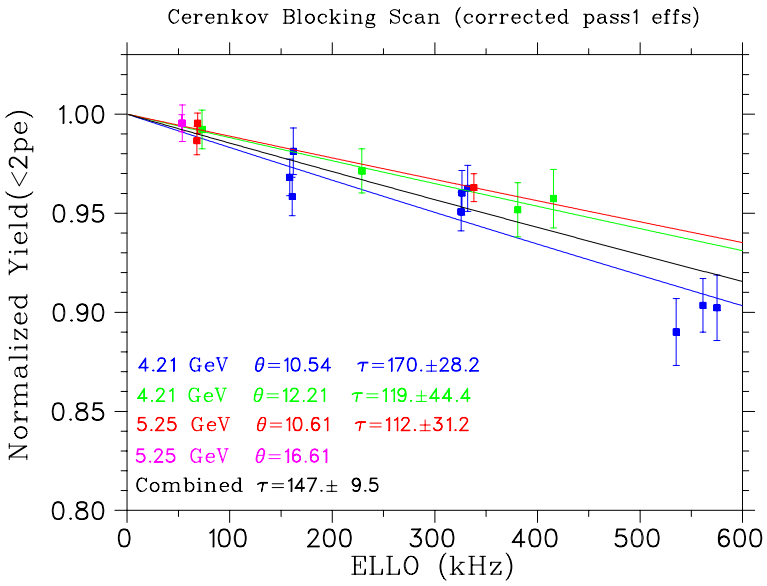

FIG. 18 Normalized experimental yields as a function of HMS singles rate, for data with SCIN-3/4 HMS trigger, with a $N_{p.e.} > 2.0$ Cerenkov particle identification cut applied. The tracking efficiency and cryotarget boiling corrections discussed in Secs.II.C.2,II.D are applied. The colored lines are fits of the form $Y = Ae^{-R\tau}$ for each kinematic setting separately. The black line is a combined fit to all of the data, as explained in the text.

The $E_e = 5.25$ GeV, $\theta_{HMS} = 16.61$ setting was then normalized to the lowest rate run of the $E_e = 5.25$ GeV, $\theta_{HMS} = 10.61$ setting. The combined fit to the renormalized data is shown by the black line in Fig. 18. The combined fit unavoidably depends on the renormalization constants chosen for the four kinematic settings, but the methodology employed does not allow too much arbitrary judgment.

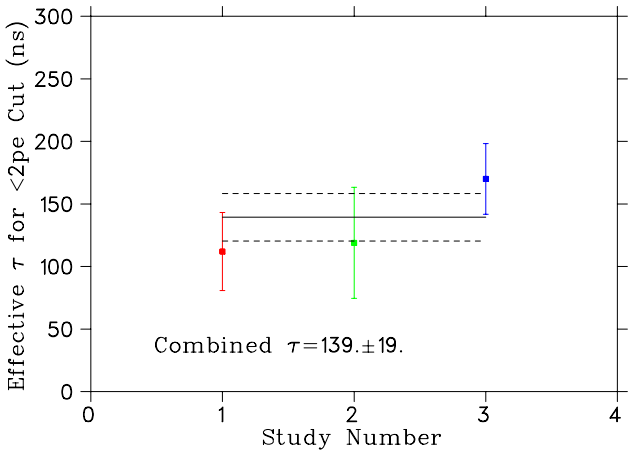

FIG. 19 Effective Cerenkov gate widths for the $hcer_{npe} < 2.0$ cut used in the F_π-2 data analysis, color coded according to the fits versus rate in Fig. 18. The black line is the error-weighted average, while the dashed lines indicate the uncertainty.

The Cerenkov blocking τ_{eff} value and its uncertainty was estimated from the fits to the three kinematic settings shown in Fig. 18. Note that these fits depend sensitively upon the tracking efficiency and cryotarget boiling corrections used. Taking into account the respective uncertainties in these fits yields a central value of 139 ± 19 ns.

Since this τ value was determined with singles events, it needs to be adjusted to yield the effective gate width for coincidence events. As discussed in Sec. II.E.1, the region to the left of the main peak in Figs.14-16 corresponds to early electrons passing through the detector before the electrons associated with the trigger, already addressed in the coincidence time blocking correction. The correction factor is the ratio of the time from the notch to the left of the main peak (Chan 900) to the right edge of the plateau (Chan 2050), divided by the time of the full distribution (Chan 425 to Chan 2050),

$$\frac{116.4 \pm 6.3 \text{ ns}}{162.9 \text{ ns}} = 0.714 \pm 0.039. \tag{13}$$

Multiplication by this factor gives $(139 \pm 19) \times (0.714 \pm 0.039) = 99.2 \pm 19$ ns.

The two F_π-2 Cerenkov blocking studies (TDC gate width of 116.4 ± 6.3 ns and corrected singles value of 99.2 ± 19 ns) are statistically consistent. It is difficult to tell which one is more definitive, so the error weighted average $\tau_{eff} = 114.7 \pm 6.0$ ns, is used to compute the Cerenkov blocking correction

$$\delta_{CCblock} = e^{-ELLOrate * \tau_{eff}}. \tag{14}$$

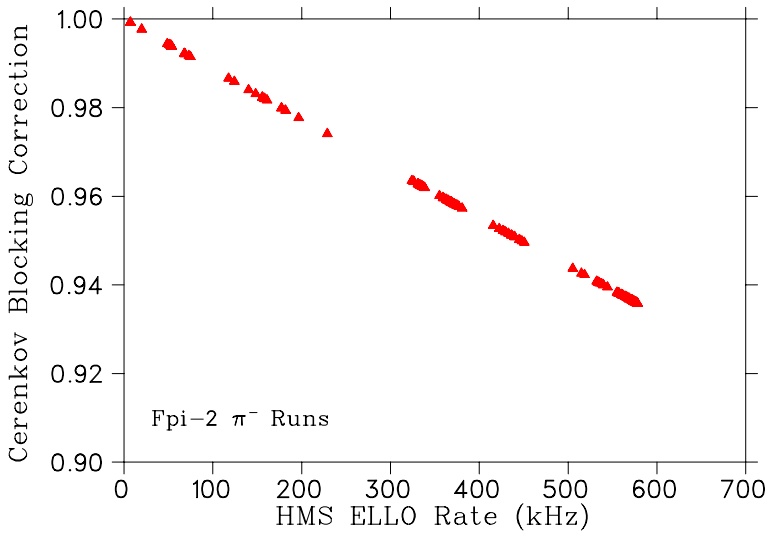

FIG. 20 F_π-2 HMS Cerenkov blocking correction $\delta_{CCblock}$ plotted as a function of the HMS electron singles rate for the $Q^2 = 2.45$ GeV^2 setting. The purpose of this plot is to show the range of blocking corrections applied, and their frequency of application.

appropriate for the F_π-2 π^- analysis. This correction is shown as a function of the HMS electron singles rate in Fig. 20. The ± 6.1 ns uncertainty at 500 kHz gives an uncorrelated systematic uncertainty of 0.3%, while the 17 ns difference in τ values from the two methods gives a scale uncertainty of 0.8%.

3. Cerenkov Blocking Correction for F_π-1 Data

Open trigger data at different electron rates were unfortunately not taken during the F_π-1 experiment, so the Cerenkov blocking correction cannot be directly determined for those data. We therefore modify the Cerenkov blocking correction determined from F_π-2 data for use in the F_π-1 analysis according to the following procedure.

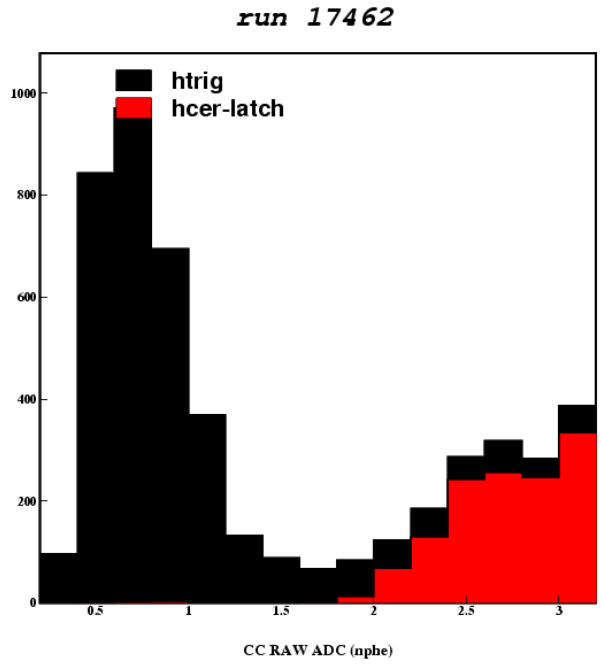

FIG. 21 A summed photoelectron histogram from the HMS Cerenkov for a representative F_π-1 carbon elastics run, $^{nat}C(e,e')$. The Cerenkov veto is not in the trigger; those events which would have most likely been vetoed (as determined from a nonzero Cerenkov trigger TDC value) are indicated in red. The effective veto threshold appears to be at about 2 photoelectrons.

Fig. 21 shows a HMS Cerenkov photo-electron histogram for a carbon elastics run taken at the very beginning of F_π-1, immediately before the first π data run. It indicates that the effective veto threshold in the F_π-1 experiment is slightly lower than that used in F_π-2. Therefore, a slightly more restrictive software threshold of $hcer_{npe} < 1.5$ was applied in the analysis of the F_π-1 data. The figure also indicates that the Cerenkov veto would be about 80% efficient for this run. Very few

timing checks were performed after the initial experimental setup, and our investigations indicate that the Cerenkov veto efficiency varied with kinematic setting during the F_π-1 experiment.

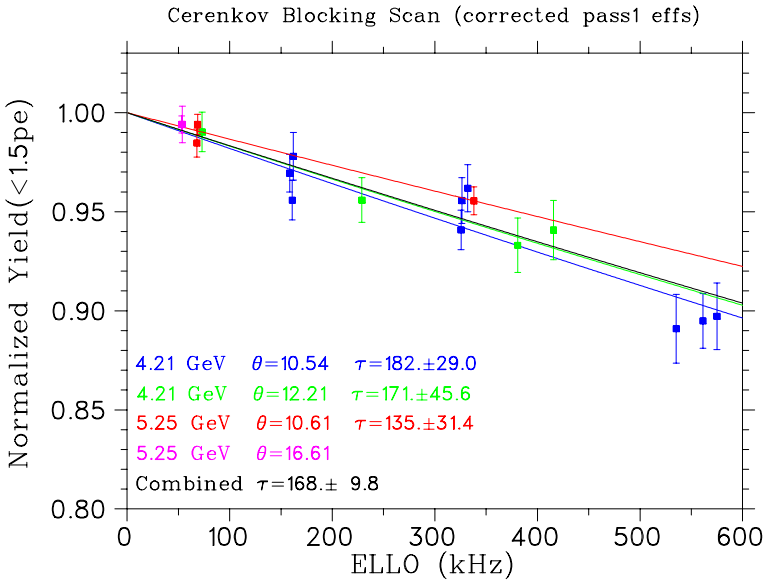

FIG. 22 The data are the same as in Fig. 18, except that a $N_{p.e.} > 1.5$ Cerenkov particle identification appropriate to the F_π-1 analysis is applied.

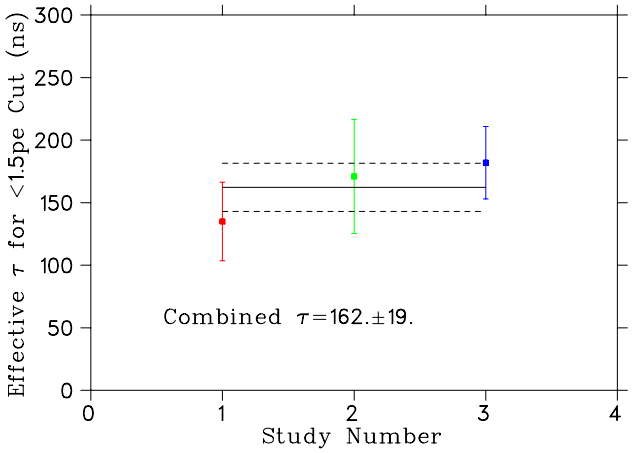

FIG. 23 Effective Cerenkov gate widths determined from F_π-2 data, but with a $hcer_{npe} < 1.5$ cut appropriate for the F_π-1 data analysis.

We therefore reanalyzed the F_π-2 dedicated π^- runs with SCIN-3/4 trigger, except that a $N_{p.e.} > 1.5$ Cerenkov particle identification appropriate to the F_π-1 analysis was applied, and obtained the results shown in Figs. 22,23. Taking into account the respective uncertainty in these three fits yields a central value of $\tau = 162 \pm 19$ ns, which is then corrected by Eqn. 13 to give $\tau = (162 \pm 19) \times (0.714 \pm 0.039) = 115.7 \pm 20$ ns.

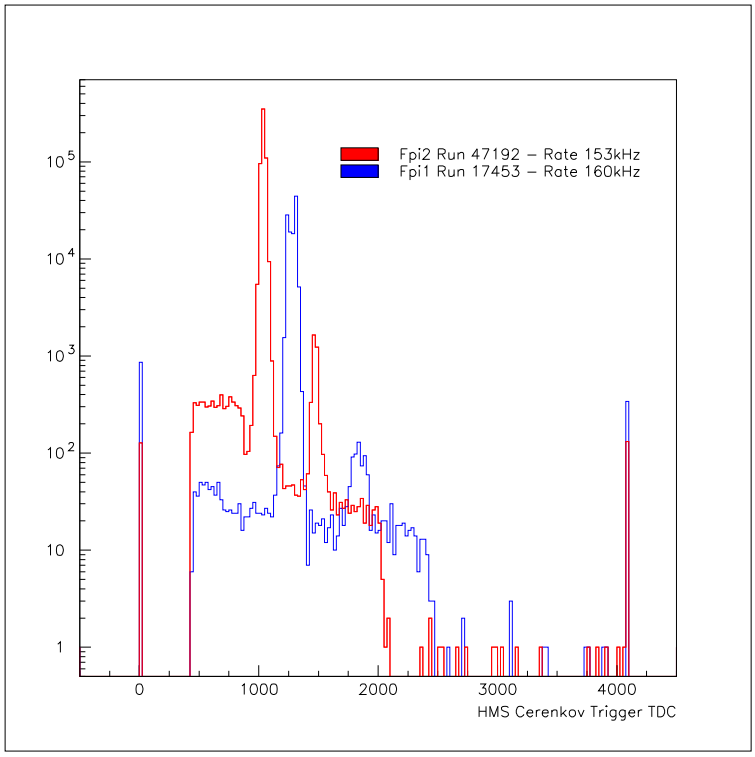

FIG. 24 Cerenkov Trigger TDC histogram for the one F_π-1 π^- run with SCIN-3/4 trigger (blue), compared to a F_π-2 SCIN-3/4 run at similar rate (red). HMS singles events, subject to a $N_{p.e.} > 2.0$ Cerenkov cut, are used in both spectra. The TDC scale is 100 ps/chan.

Finally, we used the TDC timing information from the only F_π-1 "open trigger" SCIN-3/4 run taken just before the main data taking to estimate the scaling with respect to the F_π-2 timing information. As shown in Fig. 24, the TDC timing window used during F_π-1 is wider than in F_π-2. Comparing the time from the notch to the left of the main peak to the edge of the plateau in the F_π-2 spectrum (116.4 ± 6.3 ns) to the equivalent features in the F_π-1 spectrum (138.4 ± 6.3 ns), indicates a scale factor of 1.19 ± 0.084. Application of this scale factor to the τ value determined from the F_π-2 data yields $\tau = (115.7 \pm 20) \times (1.19 \pm 0.084) = 137.7 \pm 26$ ns.

The two values compare well and thus the error-weighted average $\tau_{eff} = 138.4 \pm 6.1$ ns of the two was taken as the effective τ value to compute the Cerenkov blocking corrections for the F_π-1 data normalization. These values are shown as a function of the electron rate in Fig. 25. The ± 6.1 ns uncertainty at 1.2 MHz gives an uncorrelated systematic uncertainty of 0.7%, and scaling the 0.8% F_π-2 scale uncertainty to 1.2 MHz gives a scale uncertainty of 1.0%.

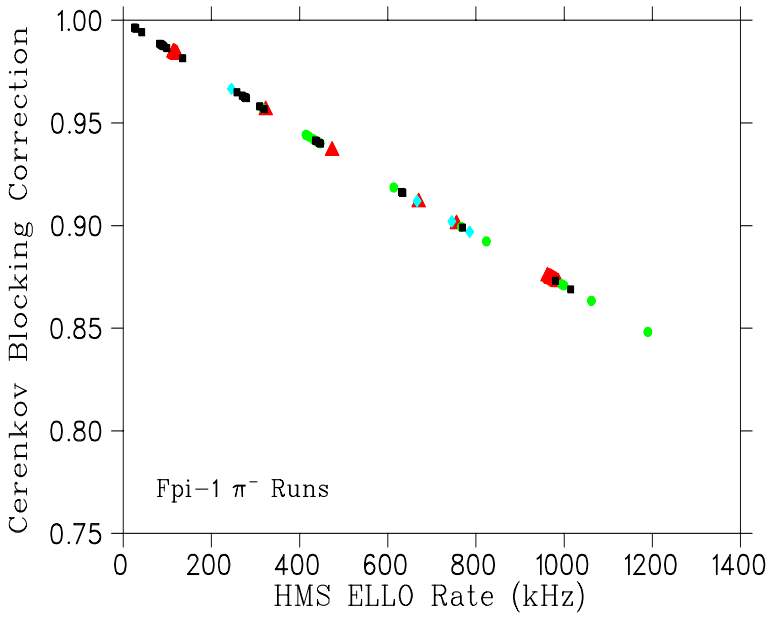

FIG. 25 F_π-1 HMS Cerenkov blocking correction $\delta_{CCblock}$ plotted as a function of the HMS electron singles rate. Note that the maximum HMS singles rate was much higher in F_π-1 than F_π-2. The plotting symbols indicate the Q^2 setting as follows: [red triangle] $Q^2 = 0.6$; [cyan diamond] $Q^2 = 0.75$; [green circle] $Q^2 = 1.0$; [black square] $Q^2 = 1.6$ GeV^2. The purpose of this plot is to show the range of blocking corrections applied, and their frequency of application.

F. F_π-2 Yield Ratio Study

The five pairs of π^- runs identified in Table V, where for each pair the beam and rate conditions were identical but the HMS trigger conditions different, can be used to probe additional rate dependent effects. The ratios of normalized yields

$$R = \frac{N_{\pi^-\_run\_with\_veto}}{N_{\pi^-\_run\_without\_veto}} \tag{15}$$

were thus formed, using the $N_{p.e.} < 2.0$ data (columns S2 and C2) in Table V. As indicated from the values in the table, the uncertainty in the tracking efficiency and target boiling corrections cancel in the ratio, which depends only on the knowledge of the cpu livetimes and prescale factors. These ratios are plotted versus rate in Fig. 26. The effective gate width determined from this study, determined from a fit that is constrained to unity at zero rate, is $\tau = 91 \pm 22$ ns, while a fit without this constraint gives $\tau = 37 \pm 37$ ns. This indicates a small residual rate dependence due to additional trigger level effects not otherwise accounted for in the analysis. Since the prescale factors should be known, presumably this is due to the cpu livetime. It is sometimes observed that heavily prescaled singles events encounter a different cpu livetime than coincidence events. It seems likely that the residual rate dependence of the singles ratios shown in Fig. 26 is due to this

issue. Without accurate information on the singles cpu livetime we cannot proceed further. We note that studies of this nature would be a valuable tool in our planned 12 GeV experiments, and we should aim to acquire better data to allow a more complete study in the future.

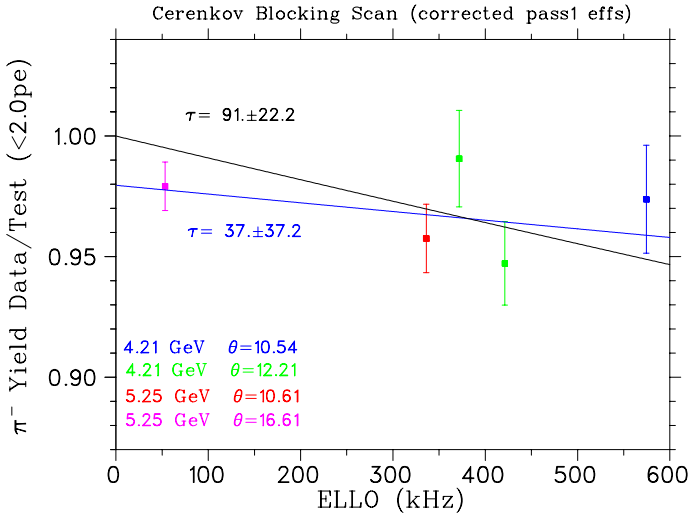

FIG. 26 Yield ratios versus HMS singles rate for π^- runs where the Cerenkov veto was included in the HMS trigger, divided by the corresponding run at same current and rate where the HMS trigger was SCIN-3/4. A 1% systematic uncertainty has been added in quadrature to all ratio error bars.

G. HMS Beta Cut Correction

In the main analysis package, β is the velocity of the detected charged particle determined from the time of flight between the two scintillator hodoscopes in the detector stack. The coincidence time spectrum at low β (Fig. 27) displays a "tail" due to pions undergoing nuclear interactions in the scintillators, Cerenkov detector material, and in the case of F_π-2 experiment the Aerogel Cerenkov detector material which was absent during F_π-1. These scattered pions have a larger time of flight. There are also events with $\beta = 0$, which means that no hits in the relevant scintillators were found when projecting the reconstructed track to the hodoscopes.

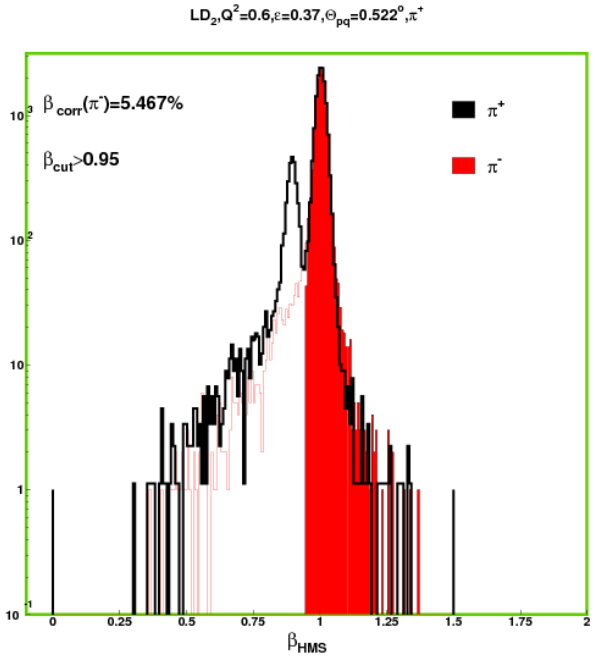

FIG. 27 β_{HMS} spectrum for the π^- channel (red thin line) and the π^+ channel (black thick line), scaled with respect to each other, and overlapped with the β_{HMS} region defined by the $\beta > 0.95$ cut (solid area) for one of the F_π-1 kinematic settings. The second peak at lower β present only in the π^+ data is due to protons.

Due to the fact that the Aerogel Cerenkov detector was not yet in existence at the time of the F_π-1 experiment, it was not possible to cleanly eliminate the proton background which contaminated the π^+ data set. In order to reduce the proton contamination of π^+ data set, we applied a beta

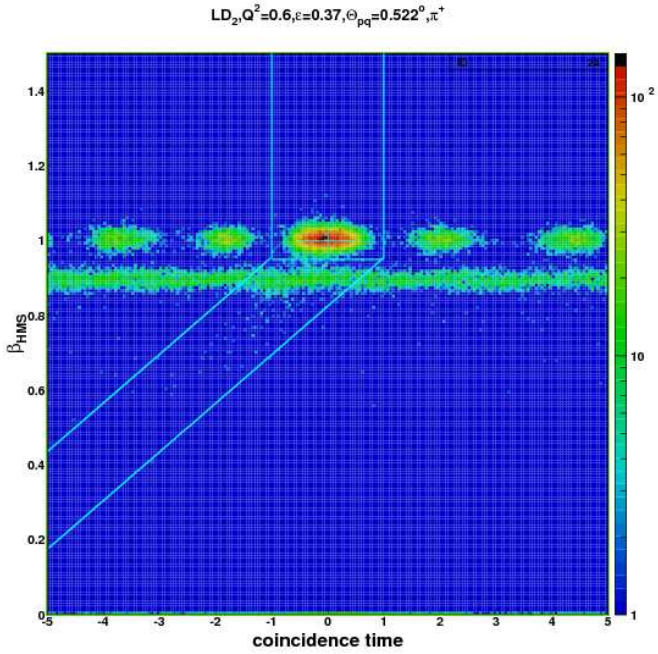

FIG. 28 Coincidence timing spectrum plotted versus β for the F_π-1 data set. In Ref. (9) it was verified that the β tail is caused by late hits in S2 rather than early hits in S1 by comparing TOF to coincidence timing. This supports the idea that there is an interaction in S1 (with the expected timing) and the particle that hits S2 is either slower or deviates from the near detectir-perpendicular trajectories, yielding a later S2 time. The solid lines indicate the cuts applied on both variables in order to select "good electrons" as well as to compute the β cut correction.

cut $\beta > 0.95$, as shown in Fig. 27. The so called "beta cut correction" was defined as the ratio of the "blob" (defined by the following cuts: $-1 <$ coincidence timing < 1 and $\beta > 0.95$), and "blob" plus "tail" as shown in the Fig. 28. This correction was extracted from π^- data and applied to both data sets (π^+ and π^-) as a normalization constant to account for the pions lost due to this cut. The β cut correction used in the final F_π-1 normalization was 4.89% with an uncertainty of 0.41% determined from the standard deviation, as indicated at the bottom of Table VI.

For the F_π-2 data set, the same procedure was used, but adjusted for the presence of the Aerogel Cerenkov detector. This permitted the separation of protons from pions, leading to a much cleaner pion sample (Fig. 29). For each π^+ and π^- kinematic setting, "beta cut corrections" were extracted in the same fashion as explained earlier (see Fig. 30). The corrections are summarized in Table VII. The β cut corrections applied in the final F_π-2 normalization are the $2.42\% \pm 0.12\%$ and $2.51\% \pm 0.18\%$ average values determined for π^+, π^+, respectively.

Kin	Q^2	ϵ	$\theta_{pq}[deg]$	β_{cut} corr. [%]
1	0.6	0.37	0.5	5.46
2	0.6	0.37	4	5.42
3	0.6	0.74	0	4.81
4	0.75	0.43	0	5.11
5	0.75	0.43	4	4.69
6	1.0	0.33	0	5.02
7	1.0	0.33	4	4.57
8	1.0	0.65	0	5.23
9	1.6	0.27	0	5.05
10	1.6	0.27	4	4.09
11	1.6	0.63	-4	5.04
12	1.6	0.63	0	4.80
13	1.6	0.63	4	4.27
Mean				4.89 ± 0.41

TABLE VI β_{cut} corrections for the π^- channel for each of the 13 F_π-1 kinematic settings. Note that the correction was applied as a normalization constant for each kinematic setting separately.

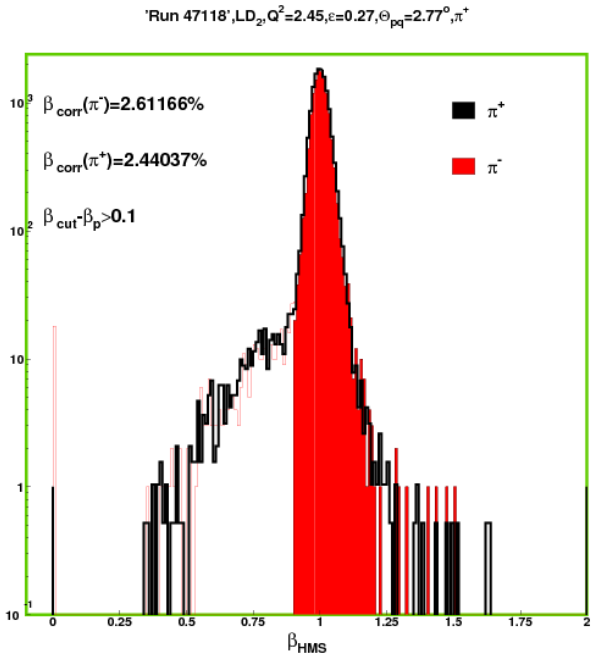

FIG. 29 β_{HMS} spectrum for π^- (red thin line) channel and π^+ (black thick line) channel, scaled with respect to each other, and overlapped with the β_{HMS} region defined by the $\beta > 0.95$ cut (solid area) for one of the F_π-2 kinematic settings.

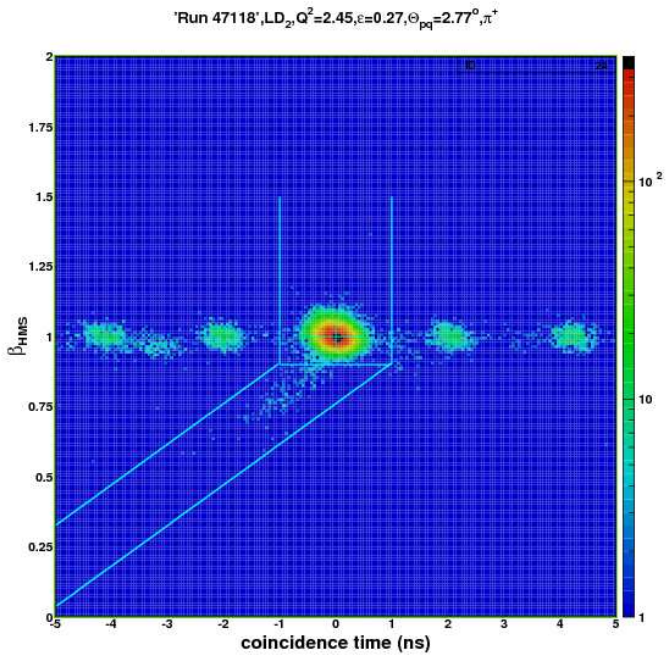

FIG. 30 Coincidence timing plotted versus the β of the detected charged particle for the F_π-2 data set. The solid lines indicate the cuts applied on both variables in order to select "good pions" as well as to compute the β cut correction.

Kin	Q^2 ϵ θ_{pq}	β_{cut} corr. [%]
π^+ Settings		
1	2.45 0.27 1.35	2.44
2	2.45 0.27 3	2.59
3	2.45 0.54 0	2.30
4	2.45 0.54 3	2.30
5	2.45 0.54 -3	2.45
Mean		2.42 ± 0.122
π^- Settings		
1	2.45 0.27 1.35	2.61
2	2.45 0.27 3	2.60
3	2.45 0.54 0	2.71
4	2.45 0.54 3	2.33
5	2.45 0.54 -3	2.31
Mean		2.51 ± 0.179

TABLE VII β_{cut} corrections for each of the F_π-2 kinematic settings.

H. Pion Absorption in the HMS

A fraction of the produced pions are lost as a result of nuclear interactions in the materials that they traverse before reaching the HMS detectors. For the pion momenta used in F_π-1,2, the dominant pion reaction types are the inelastic scattering and charge exchange processes, resulting in a deflection and loss of momentum of the pion, and the pion absorption process, resulting primarily in the emission of energetic protons and neutrons. The proportion of pions lost due to these processes must be correctly accounted for. The situation is complicated by the fact that pion absorption in the scintillators, aerogel, and Cerenkov detector material leading to the emission of energetic protons are already included in the β-cut correction. The pion absorption correction is intended to account for the HMS triggers that are lost due to pion interactions in materials upstream of the drift chambers, or interactions in the detector stack such as large angle deflection, or absorption processes leading to the emission of only low momentum or neutral particles, which do not give enough signal in the scintillators providing the trigger.

To study the interplay between the pion absorption and β-cut corrections, the transmission of pions from the target through to S2X was calculated and used to estimate which fractions of these end up in the various parts of the β versus coincidence time spectrum. The pion transmission for each material was calculated by making use of their known areal densities and the nuclear collision lengths λ from Ref. (10). Since these λ values are only appropriate for high energy particles, where the energy dependence is small, they were rescaled according to the energy dependence of the $\pi^+ p$ interaction. It was assumed that all pion reactions from the target to spectrometer exit window resulted in lost triggers. For the pions reacting from the drift chambers to S1, it was assumed that a fraction f_1 were lost triggers, while the remaining $1 - f_1$ were not lost, but ended up with either $\beta = 0$ (meaning no valid track was found by the tracking algorithm) or in the 'tail' (β below the cut value). Finally, for the interactions from the Cerenkov through to the first 1/4 thickness of S2 (corresponding to approximately the deposition necessary to cause a trigger), it was assumed that fraction f_2 resulted in a low β value, while the remaining $1 - f_2$ were indistinguishable from those pions that did not undergo nuclear reactions.

To determine the fractions f_1, f_2 appropriate for the F_π-1,2 deuterium data, the following procedure was employed. The fractions of $\beta = 0$, 'tail' and 'blob' events were determined for each F_π-1 π^- setting, and for each F_π-2 π^- and π^+ setting (see Fig. 31). Since low β values could also be due to instrumental timing effects, the same proportions were also determined from representative F_π-1,2 runs with electrons in the HMS. The electron fractions were then subtracted

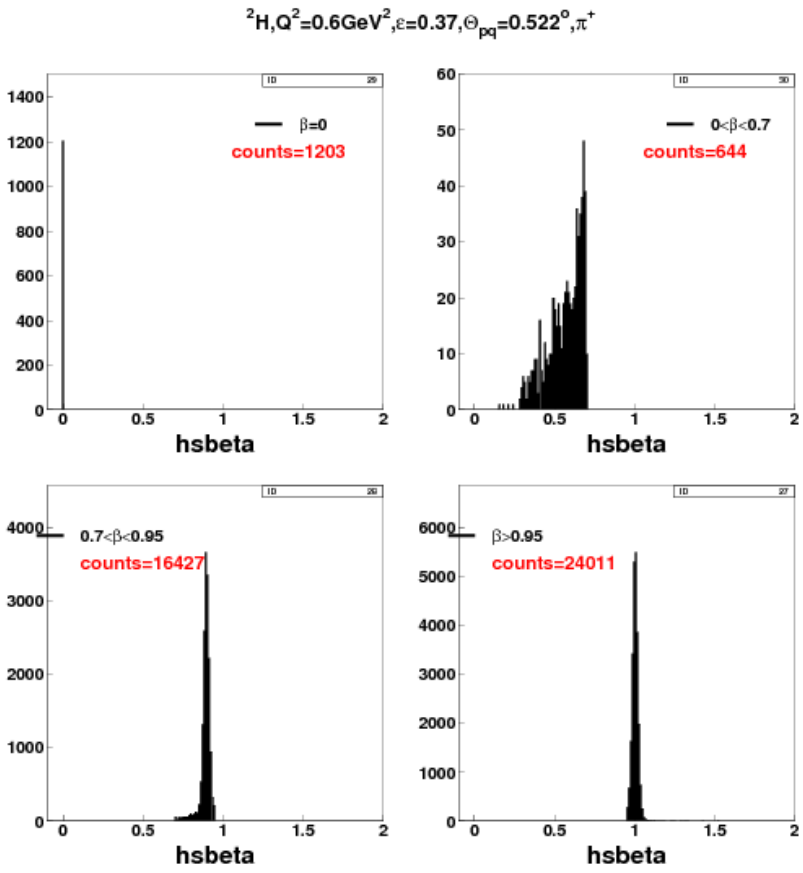

FIG. 31 HMS β spectrum for a representative π^+ run in F_π-1, showing the proportion of HMS events with $\beta = 0$, the proportions in the 'low' ($0 < \beta < 0.7$) and 'high tails' ($0.7 < \beta < 0.95$), and those in the 'blob' ($\beta > 0.95$). To avoid proton contamination due to the lack of an Aerogel Cerenkov detector in F_π-1, the higher cut value of $\beta = 0.95$ was used to define the 'blob' and 'tail' regions in the calculation of the pion absorption correction.

from the pion fractions, yielding typical 'zero+tail' values of 2.2+4.0=6.2% (2.6+2.2=4.8%) for F_π-1 (F_π-2), with the remainder in the 'blob'. f_1, f_2 were then inferred by comparison of the observed 'zero+tail' values to the calculated interaction probabilities. For F_π-1, the calculation predicted too few zero+tail events and too many in the blob, with the closest agreement being for the assumption that none of the interacting pions resulted in lost triggers ($f_1 = 0$), and 100% of

the interacting pions ended up in the 'zero+tail' ($f_2 = 1$). For F_π-2, values of $f_1 = 0.3 - 0.45$ and $f_2 = 0.75 - 1.0$ resulted in good agreement with the data.

The calculated interaction probability from the target to exit window was 0.55% for F_π-1, and 0.70% for F_π-2, where the higher F_π-2 value is mainly due to the thicker titanium spectrometer exit window and the addition of the aerogel Cerenkov in the detector stack. For F_π-1, we then conservatively estimated from the 0.55% target to exit window contribution, and the 'zero interacting pions' from Cerenkov to S2, a pion 'absorption' (lost trigger) correction of $1\% \pm 1\%$. Following a similar procedure for F_π-2 yielded an estimated correction of $2\% \pm 1\%$.

I. Data Corrections Summary

Summary of F_π-1 Correction Factors	
HMS tracking efficiency correction	$1 - (0.0676 \pm 0.002)/\text{S1Xrate(MHz)}$
LD_2 Cryotarget Boiling	$1 - (0.0472 \pm 0.003)/100\mu\text{A}$
Beam Current Offset	0.2μA
HMS Cerenkov blocking	$e^{-\text{ELLOrate}*(138.4\pm6.1\text{ns})}$
β_{cut} correction ($\pi^\pm$)	$4.89\% \pm 0.41\%$
Pion Absorption	$1\% \pm 1\%$
SOS Cerenkov efficiency	$99.92\% \pm 0.02\%$ (8)
SOS Calorimeter efficiency	$99.5\% \pm 0.1\%$ (8)
HMS Cerenkov efficiency	$99.6\% \pm 0.05\%$ (8)
Coincidence Time Blocking	$e^{-\text{TotalPretrigrate}*(140\text{ns})}$ (6)
HMS electronic live time	$1 - 5/6(hEL60 - hEL120)/hELREAL$ (6)
SOS electronic live time	$1 - 5/6(sEL60 - sEL120)/sELREAL$ (6)
Summary of F_π-2 Correction Factors	
HMS tracking efficiency correction	$1 - (0.0676 \pm 0.002)/\text{S1Xrate(MHz)}$
LD_2 Cryotarget Boiling	No correction. $\pm 0.3\%/100\mu A$
HMS Cerenkov blocking	$e^{-\text{ELLOrate}*(114.7\pm6.0\text{ns})}$
β_{cut} correction (π^-)	$2.51\% \pm 0.18\%$
β_{cut} correction (π^+)	$2.42\% \pm 0.12\%$
Pion Absorption	$2\% \pm 1\%$
SOS Cerenkov efficiency	$99.92\% \pm 0.02\%$ (8)
SOS Calorimeter efficiency	$99.5\% \pm 0.1\%$ (8)
HMS Cerenkov efficiency	$99.6\% \pm 0.05\%$ (8)
HMS Aerogel efficiency	$99.5\% \pm 0.02\%$ (8)
Coincidence Time Blocking	$e^{-\text{SOSPretrigrate}*(92\text{ns})}$ (8)
HMS electronic live time	$1 - 6/5(hPRE100 - hPRE150)/hPRE100$ (8)
SOS electronic live time	$1 - 6/5(sPRE100 - sPRE150)/sPRE100$ (8)

TABLE VIII Summary of corrections applied to the deuterium data. In addition, HMS and SOS tracking efficiencies and computer live times are applied on a run-by-run basis.

III. MONTE CARLO SIMULATIONS

A. Model for Pion Electroproduction in Deuterium

Because of the role of Fermi momentum in ^{2}H, different choices can be made in the construction of a quasi-free model for pion electroproduction from deuterium.

1. Initial Quasi-Free Model

The first two analyses of our ^{2}H data made use of the model presented in detail in Ref. (9). In this model, pion electroproduction is assumed to follow a quasifree process, where the pion is produced from an interacting proton (or neutron in the case of π^- production) with some initial momentum coming from the Fermi motion in the nucleus. The cross section is six fold, so six quantities must be generated for each simulated event, the additional variable (compared to ^{1}H) being the missing mass. The variables of choice are the spectrometer in-plane and out-of-plane angles for both the electron and pion arms (SOS and HMS spectrometer angles), the final electron energy, and the final pion momentum. The deuterium wave function is based on a Bonn potential calculation (11), while the nucleon momentum is generated according to the Fermi momentum distribution with the direction being generated uniformly in cosθ and ϕ in the nucleus rest frame.

Due to the fact that the struck nucleon is bound in the nucleus and its energy is not uniquely specified by its momentum, an off-shell prescription was chosen to fully determine the kinematics. The "spectator" nucleon was taken to be "on-shell" in the initial state, while the struck nucleon was taken to be "off-shell" with the requirement that the total momentum of the nucleus is zero, and the total energy is the mass of deuterium, M_D.

$$E_{struck} = M_D - \sqrt{m^2_{spectator} + p^2_{Fermi}}, \tag{16}$$

where $m_{spectator}$ is the on-shell spectator nucleon mass and p_{Fermi} is the momentum of the struck and spectator nucleons.

Another ingredient used in this model is the Jacobian that accounts for the fact that the events are generated in spectrometer coordinates instead of physics coordinates. Thus, one needs to calculate the transformation that takes the reference system of coordinates for this reaction from the center of mass to the lab system. The Jacobian of the cross section transformation is given in Appendix B of Ref. (9). The resulting five-fold cross section can be written as the virtual photon

cross section times the virtual photon flux Γ,

$$\frac{d^5\sigma}{d\sigma_e dE_e d\Omega_\pi dP_\pi} = \Gamma \frac{d\sigma}{d\Omega_\pi dP_\pi}. \tag{17}$$

The CM frame in this case is that of the virtual photon and moving struck nucleon. The angles θ_{CM} and ϕ_{CM} cannot be reconstructed for the experimental data, because they depend on the the Fermi momentum of the struck nucleon, which is not known for an experimental event. (Note that, due to the Fermi momentum, $\phi_{CM} \neq \phi_{\pi q}$, where $\phi_{\pi q}$ is the azimuthal angle in the lab frame between the q-vector and the outgoing pion.) But these angles are used in the SIMC quasi-free physics generator, where the virtual-photon cross section is calculated via

$$\frac{d\sigma}{d\Omega_\pi} = \frac{d\sigma_T}{d\Omega_\pi} + \epsilon \frac{d\sigma_L}{d\Omega_\pi} + \sqrt{2\epsilon(1+\epsilon)} \frac{d\sigma_{LT}}{d\Omega_\pi} cos\phi_{CM} + \epsilon \frac{d\sigma_{TT}}{d\Omega_\pi} cos2\phi_{CM}, \tag{18}$$

where σ_L, σ_T, σ_{LT}, and σ_{TT} are the usual separated response functions, which depend on θ_{CM}.

The SIMC data are reconstructed in a manner similar to that of the experimental data, except that for the experimental data a different θ'_{CM} is used, by boosting to the photon plus fixed nucleon target system instead of the photon plus moving nucleon system. The simulated yields are calculated and binned versus $\phi_{\pi q}$, $-t$ and compared to the experimental yields for the same bins. In order to alleviate problems such as the averaging over the phase space of each $-t$ bin and the need for L/T separation to have the same values for W, Q^2, and $-t$ at high and low ϵ, a model was created such that the ratio of experimental Y_{exp} to simulated Y_{sim} yields does not depend (or hardly depends) on W, Q^2, $-t$, θ and ϕ.

$$\left(\frac{d\sigma}{dt}\right)_{exp} = \frac{Y_{exp}}{Y_{sim}} \left(\frac{d\sigma}{dt}\right)_{MC}. \tag{19}$$

The iterative fitting procedure used to create the model for the cross section is described in Sec. III.D

2. Final Quasi-Free Model

The model described in the previous section has the virtue that the used cross section presumably is closest to the one used in the ^{1}H analysis. However, the finally determined cross section will depend on the assumed distribution of the Fermi momentum of the nucleon in the deuteron, and, perhaps more awkward, there is no direct relation between the separated response functions used in the SIMC model (Eqn. 18) and the experimentally determined ones, which are determined using the angles θ'_{CM} and $\phi_{\pi q}$, while also the values of t, W, on which they depend, are not the same. The latter is illustrated in Fig. 32. The large spread is due to k_F having different values in the

various events. It should be mentioned that this large spread is greatly reduced when integrating over k_F, but the connection between the two sets of response functions mentioned and thus the fitting of the response functions remains complicated.

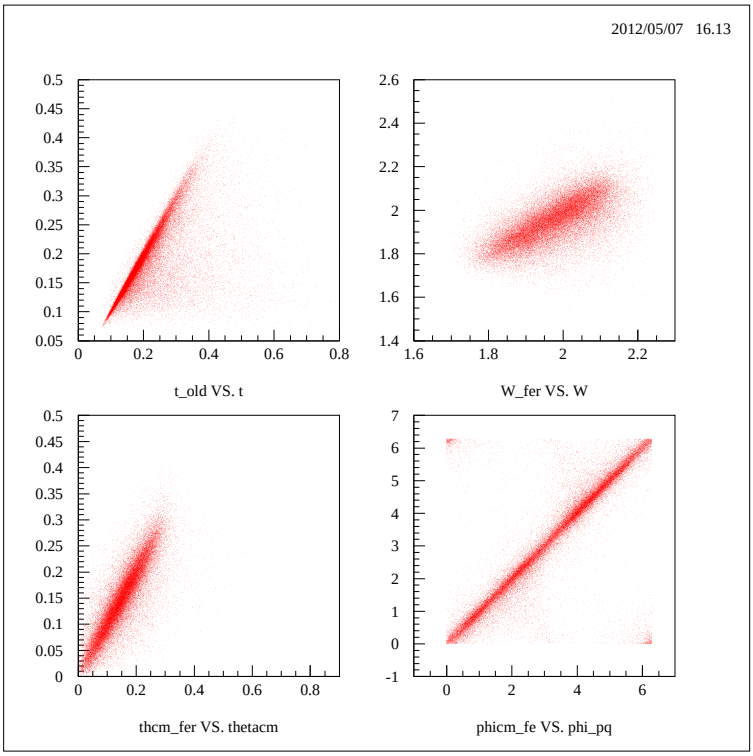

FIG. 32 Comparison of kinematic variables of events in the initial SIMC model (y-axis) versus the final SIMC model (x-axis) for the π^+ setting $Q^2 = 1.6$ GeV^2, $\epsilon = 0.63$, $\Theta_{\pi q} = 0$.

For these reasons, we ultimately decided to use in the SIMC physics reconstruction the same simple quasi-free model as used in the experimental data reconstruction, i.e., we assume that the virtual photon interacts with a nucleon, which is at rest. In that case ϕ_{CM} equals the experimentally reconstructed $\phi_{\pi q}$ and θ_{CM} is calculated by boosting to the photon plus nucleon at rest system, as was also the case for the ^{1}H analysis. In this way the SIMC reconstruction and the experimental data reconstruction are completely consistent with each other and people who later want to look into or use our cross sections know exactly how they are defined and have been detemined.

The SIMC event generator still incorporates Fermi momentum in the generation of the particle momenta, and all off-shellness is still assumed to be with the struck nucleon. Therefore, the extracted cross sections remain sensitive to the model used, but these affects are expected to largely cancel when forming the π^-/π^+ ratios. The extracted σ_L, σ_T, σ_{LT}, and σ_{TT} are therefore effective ones, not directly to be compared to those from ^{1}H, but it is better that the influence of off-shell (and possible other mechanisms in ^{2}H) are studied separately, using cross sections that

were determined in a well defined way, than that off-shell effects are incorporated already in some way in the extracted cross sections (although the differences in practice may not be large).

In parallel with these changes to the physics model, the SIMC event reconstruction was carefully scrutinized for inconsistencies from the experimental data reconstruction. It was found that the experimental reconstruction used $t = (P_n - P_p)^2$, while the default formula used in SIMC was $t = (P_\gamma - P_\pi)^2$. In order to be consistent, $t = (P_n - P_p)^2$ was also used in all parts of SIMC, including the physics generator. In the limit of perfect resolution and no radiative effects, both formulas for t give the same result for ^{1}H, but for ^{2}H they do not, because of binding effects.

B. Simulation of Collimator Pion Punch-Through Events and Missing Mass Cut Determination

The thick collimators of the HMS and SOS are very effective in stopping electrons, but a non-negligible fraction of pions undergo multiple scattering and ionization energy loss and consequentially end up contributing to the experimental yield (9).

These pion (hadron) punch-through events have been observed in earlier experiments, and corrections are needed for a precise yield extraction. Since the pions in F_π-1 and F_π-2 are detected in the HMS, the implementation of the collimator punch-through events was done for only this arm. To account for these events, the probability that a pion interacts hadronically with the collimator (allowing the pion to undergo multiple scattering and ionization energy loss) was tested (9) and implemented in the HMS single arm Monte Carlo package as a part of the SIMC Hall C simulation software.

As can be seen in the middle panel of Fig. 33, collimator punch-through events show up in the long tail of the missing mass distribution. In accordance with the quasi-free approach, the missing mass (MM) was calculated according to:

$$\vec{p}_{missing} = \vec{q} - \vec{p}_\pi \qquad E_{missing} = \nu + m_N - E_\pi \qquad \mathrm{MM}^2 = E^2_{missing} - p^2_{missing} \tag{20}$$

where m_N equals the free proton mass for π^+ production and the free neutron mass for π^- production. In extracting the deuterium cross sections, it is desirable to keep as much of the missing-mass tail as possible (up to the two-pion threshold of 1.1 GeV), to maximize the acceptance of the "quasifree" distribution, and to minimize the systematic uncertainty associated with the missing mass cut.

After implementing the pion punch-through events in SIMC, we determined the MM cut value needed to reliably select "quasielastic" events with an electron detected in SOS and a pion detected

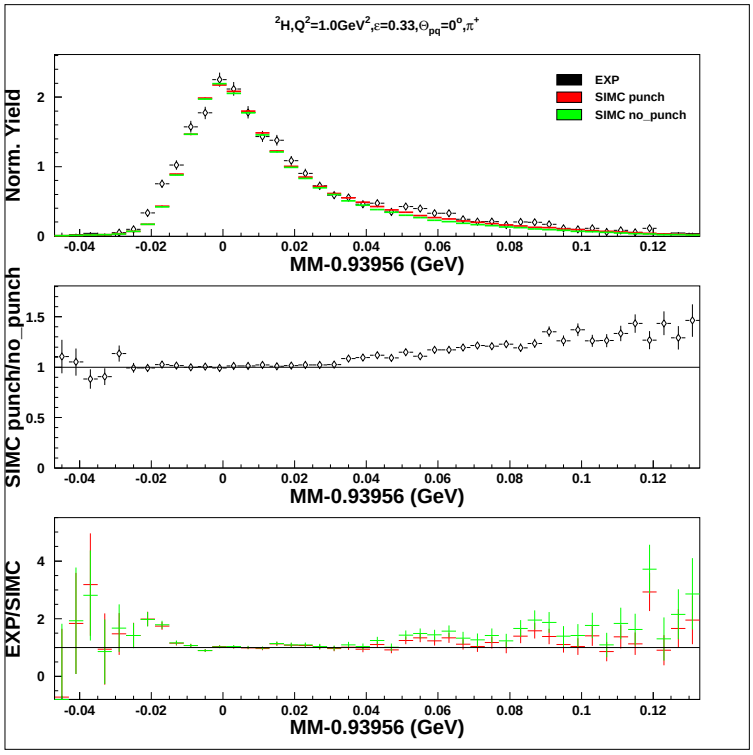

FIG. 33 Collimator pion punch-through implementation in the SIMC Monte Carlo model. The upper panel shows the normalized experimental yields (full circles), simulation yields with (red line) and without (green line) collimator punch-through implementation. The middle panel shows the ratio of the simulated data without collimator punch-through to the simulated data with this implementation. The lower panel shows the ratio of data to simulation with (red crosses) and without (green crosses) collimator punch-through implementation.

in HMS. The MM is expected to approach the "spectator" nucleon mass (proton mass m_p for π^- and neutron mass m_n for π^+ electroproduction processes). The final MM cut used in the analysis was $0.875 < \mathrm{MM} < 1.03$ GeV.

C. Selection of t Bins for F_π-1 π^- Data

Because of problems encountered during the running of the F_π-1 experiment, only the central HMS angle data were acquired for the π^- high ϵ Q^2=0.6 and 1.0 GeV^2 settings. This led to inadequate ϕ coverage at larger $-t$, degrading the reliability of the L/T separations for those kinematics. To determine the appropriate ranges in $-t$ for which reliable separated cross sections could be determined in these cases, the following study was performed. Since radiative processes can allow otherwise excluded kinematic regions to be populated, the ϕ coverage of each $-t$ bin was simulated with electron radiation turned on and off. Based on the criterion that it is necessary to have a range $\phi_{norad} > 270^o$ in which the non-radiated event yield is non-zero for reliable

L/T/LT/TT separations, it was decided that the region $-t > 0.08$ GeV^2 for the Q^2=0.6 GeV^2 data (corresponding to the last $-t$ bin in the left panel of Fig. 34), and the region $-t > 0.15$ for the Q^2=1.0 GeV^2 data (corresponding to the last $-t$ bin in the right panel of Fig. 34) had inadequate ϕ coverage. These regions were completely excluded from the data analysis.

It was subsequently determined that even this ϕ coverage requirement was insufficiently restrictive to produce reliable L/T/LT/TT cross sections for all t-bins. While separated cross sections were extracted for five π^- t-bins at Q^2=0.6 and 1.0 GeV^2, the values for the highest two $-t$-bins at these Q^2 will not be published.

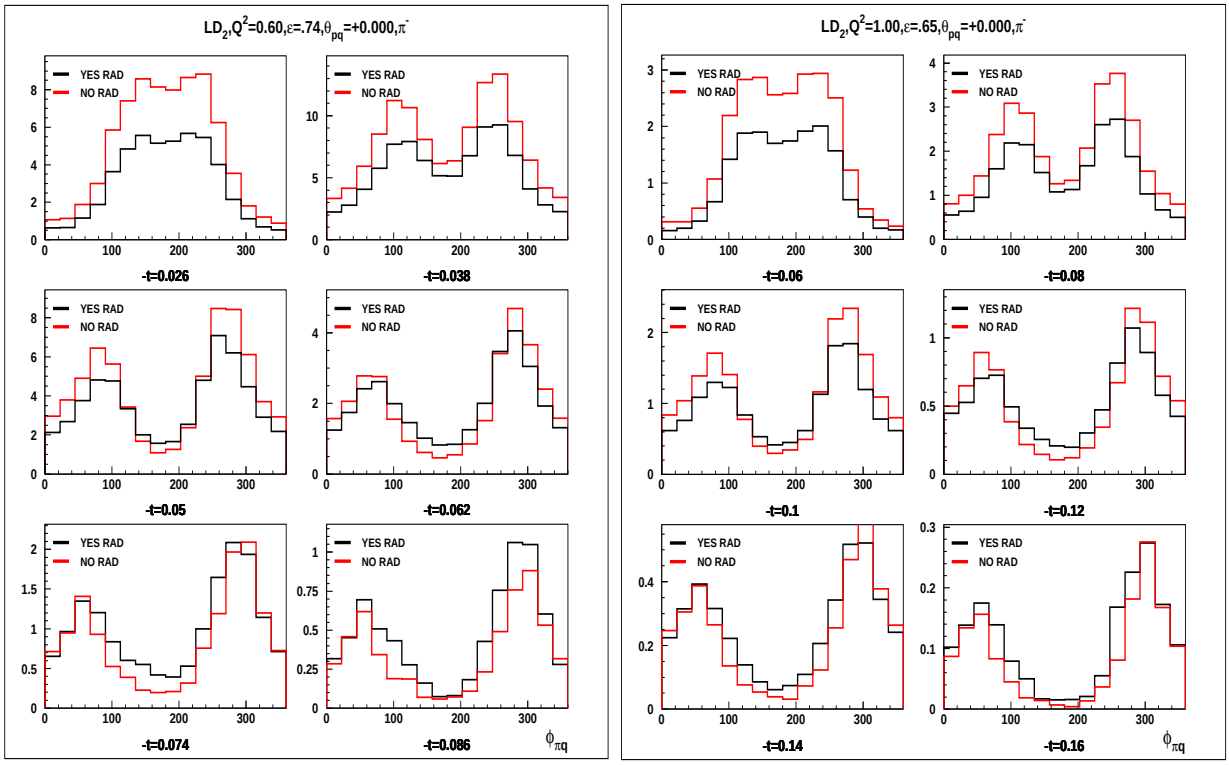

FIG. 34 Simulated ϕ coverage for the Q^2=0.6 (left panel) and 1.0 (right panel) GeV^2 high ϵ settings. Due to poor ϕ coverage ($< 270^O$), separated cross sections cannot be quoted for the last three $-t$ bins for each of these π^- settings.

D. Iteration of the Monte Carlo cross section model

The starting pion electroproduction cross section model used in the simulation was taken from previous experimental data. The individual response functions σ_L, σ_T, σ_{LT}, and σ_{TT} in the model were then optimized to follow the $-t$ and Q^2 dependences of the ^{2}H experimental data through the iterative procedure described below.

First, the ratios of experimental to simulated data were computed at every Q^2 where data were obtained, for each t, ϕ bin, and separately for each HMS central angle setting. Then these ratios were combined in a weighted average over the experimental ϕ acceptance. Using Eqn. 19, the unseparated experimental cross sections were computed for each $-t$ bin at average values $\overline{W}$, $\overline{Q^2}$ of the experimental acceptance in W and Q^2. (The same values of $\overline{W}$, $\overline{Q^2}$ were used at both ϵ settings.) Then the four response functions in the equation

$$\frac{d\sigma}{d\Omega_\pi} = \frac{d\sigma_T}{d\Omega_\pi} + \epsilon\frac{d\sigma_L}{d\Omega_\pi} + \sqrt{2\epsilon(1+\epsilon)}\frac{d\sigma_{LT}}{d\Omega_\pi}cos\phi_{pq} + \epsilon\frac{d\sigma_{TT}}{d\Omega_\pi}cos2\phi_{pq}, \tag{21}$$

were determined simultaneously by fitting the ϕ-dependences at both ϵ settings. The separated response functions σ_L, σ_T, σ_{LT} and σ_{TT} in Eqn. 21 are in fact the fit parameters. They depend on t and on W, Q^2, but as mentioned above the experimental values of σ, and thus the separated response functions, are at fixed (average) values of $\overline{W}$ and $\overline{Q^2}$. The dependence of each on W was assumed to follow the phase space factor $1/(W^2 - M_p^2)^2$ used in previous analyses of electroproduction data described in Ref. (13; 14). In addition, σ_{LT} and σ_{TT} were taken to have leading-order angular dependences of $\sin\theta_{CM}$ and $\sin^2\theta_{CM}$, respectively, where θ_{CM} is a complicated function of W, Q^2, and t. Fitting all four response functions simultaneously is advantageous, as it allows one to calculate all four terms of the cross section, including the associated uncertainties.

This method of cross-section extraction relies on the requirement that the ratio between simulated and measured yields is close to unity in all t, ϕ_{pq} bins. To ensure a reliable description of the data by the SIMC physics model, the functional forms of the separated cross sections (i.e. their t and Q^2 dependences) were fitted to the experimental cross sections using a standalone FORTRAN program which incorporates a MINUIT routine for fitting corrections to the individual response functions in a χ^2 minimization scheme (12). The thus obtained new model was then used as an input to the next iterative calculation of the experimental cross section. In this way, the Q^2 and $-t$ dependences of each of the cross section terms were iteratively determined.

The final parameterizations used for the four separated response functions in the F_π-1 π^+ analysis are:

$$\begin{aligned}
\frac{d\sigma_L}{dt} &= g(W)\Big(p_1 + p_2 ln(Q^2)\Big)e^{(p_3+p_4 ln(Q^2))(-t)}, \\
\frac{d\sigma_T}{dt} &= g(W)\Big(p_5 + p_6 ln(Q^2) + \Big(p_7 + p_8 ln(Q^2)\Big)\Big(\frac{|t| - |t_{ave}|}{|t_{ave}|}\Big)\Big), \\
\frac{d\sigma_{LT}}{dt} &= g(W)p_9 e^{p_{10}(-t)} sin\theta_{CM}, \\
\frac{d\sigma_{TT}}{dt} &= g(W)f(t)\frac{p_{11}}{Q^2}e^{-Q^2} sin^2\theta_{CM},
\end{aligned} \tag{22}$$

where $g(W) = 1/(W^2 - M_p^2)^2$ is the assumed W-dependence discussed earlier, $f(t) = -t/(-t - m_\pi^2)^2$ is the pion pole factor, $|t_{ave}|$ is the average $-t$ value for a given kinematic setting, given by $|t_{ave}| = (0.105 + 0.04ln(Q^2))Q^2$, and $p_{i=1,...,12}$ are the fit parameters.

For the F_π-1 π^- analysis, a slightly different parameterization (because σ_T and σ_{TT} showed a stronger Q^2-dependence) yielded a better fit:

$$\begin{aligned}
\frac{d\sigma_L}{dt} &= g(W)\Big(p_1 + p_2 ln(Q^2)\Big)e^{(p_3+p_4 ln(Q^2))(-t)}, \\
\frac{d\sigma_T}{dt} &= g(W)\Big(p_5 + \frac{p_6}{Q^4+0.1} + \Big(p_7 + p_8 ln(Q^2)\Big)\Big(\frac{|t| - |t_{ave}|}{|t_{ave}|}\Big)\Big), \\
\frac{d\sigma_{LT}}{dt} &= g(W)p_9 e^{p_{10}(-t)} sin\theta_{CM}, \\
\frac{d\sigma_{TT}}{dt} &= g(W)f(t)\Big(\frac{p_{11}}{Q^2} + \frac{p_{12}}{Q^4+0.2}\Big)sin^2\theta_{CM},
\end{aligned} \tag{23}$$

In the F_π-2 analyses, a common parameterization (similar to those in F_π-1) was used for both π^+ and π^-:

$$\begin{aligned}
\frac{d\sigma_L}{dt} &= g(W)\Big(p_1 + p_2 ln(Q^2)\Big)e^{(p_3+p_4 ln(Q^2))(-t-0.2)}, \\
\frac{d\sigma_T}{dt} &= g(W)\Big(p_5 + p_6 ln(Q^2) + \Big(p_7 + p_8 ln(Q^2)\Big)\Big(\frac{|t| - |t_{ave}|}{|t_{ave}|}\Big)\Big), \\
\frac{d\sigma_{LT}}{dt} &= g(W)\Big(p_9 e^{p_{10}(-t)} + p_{11}/(-t)\Big)sin\theta_{CM}, \\
\frac{d\sigma_{TT}}{dt} &= g(W)f(t)\frac{p_{12}}{Q^2}e^{-Q^2}sin^2\theta_{CM},
\end{aligned} \tag{24}$$

where $|t_{ave}| = (0.0735 + 0.028ln(Q^2))Q^2$ and $p_4 = 0$.

To summarize, the entire iteration procedure consists of five basic steps:

- use parameter values $p_{i=1,...,12}$, which occur in the formulas for the SIMC model cross section, above, to generate simulated yields, cut and binned in the same manner as the experimental data [SIMC, sim_yields.kumac],

- determine the ratios of experimental to simulated yields, Y_{exp}/Y_{sim}, for each (ϕ, t) bin [average_ratios.f, plot_r.kumac],

- calculate the unseparated experimental cross sections for each (ϕ, t) bin using Eqn. 19 [calc_xsect.f, plot_unsep.kumac],

- for each t bin, fit the ϕ-dependences at both epsilon to determine the separated cross sections [xfit_in_phi.f, plot_sep.kumac],

- fit the t-dependences of the separated cross sections to determine the set of parameter values $p_{i=1,...,12}$ to be used in the next iteration [xfit_in_t.f]

This was done for every Q^2-setting separately, keeping the parameters that describe the Q^2-dependence fixed. Then these parameters were adjusted so as to give a good description of the Q^2-dependence of the model cross section.

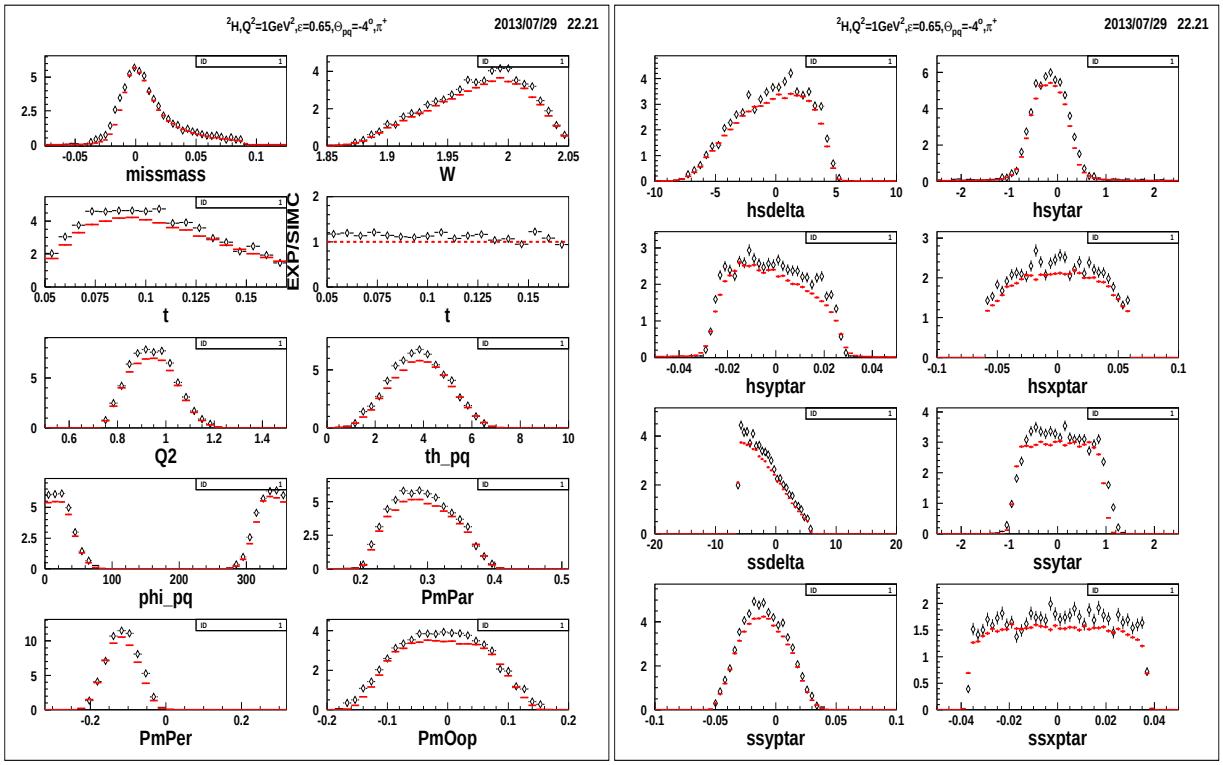

FIG. 35 Experimental (black points) to simulated (red) data comparison for various physics and HMS/SOS optical transport quantities for the π^+ setting $Q^2 = 1.0$ GeV^2, $\epsilon = 0.65$, $\Theta_{\pi q} = -4^o$.

In addition to the Y_{exp}/Y_{sim} ratios versus $-t, \phi, \theta_{CM}$, the normalized experimental yields and simulated yields for a variety of physics and HMS and SOS optical transport matrix variables were compared during the iteration process, in order to assess the quality of match between the data and the simulation. Some examples are shown in Fig. 35. The iteration procedure was repeated until satisfactory agreement between the experimental and simulated distributions was obtained, the values of $\sigma_{L,T,LT,TT}$ (and the associated fit parameters) were stable in subsequent iterations, and the parameters fitted at the individual Q^2-settings did not change much with Q^2.

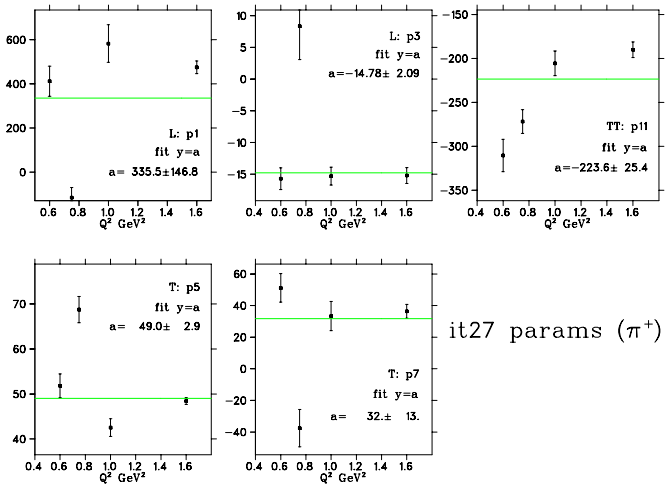

FIG. 36 Nearly final parameter values for the $F_\pi - 1$ π^+ data, plotted versus Q^2 to investigate whether the fixed parameter values in the model are appropriate. These parameters (not shown) were fixed to: $p_2 = -785$, $p_4 = 21.2$, $p_6 = -34$, $p_8 = -60$, $p_9 = p_{12} = 0$, $p_{10} = -20$. The green lines are only to guide the eye.

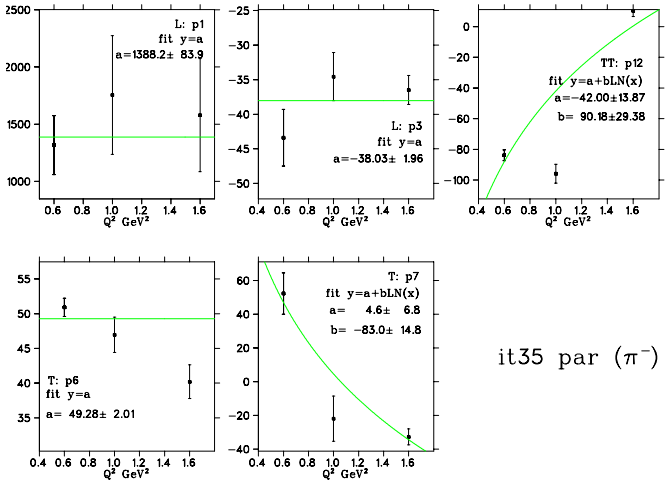

FIG. 37 Nearly final parameter values for the $F_\pi - 1$ π^- data. The parameters not shown were fixed to: $p_2 = -660$, $p_4 = 33$, $p_5 = 0$, $p_8 = 45$, $p_9 = -200$, $p_{10} = -20$, $p_{11} = 0$. Since p_7 displayed a marked Q^2-dependence, it was subsequently decided to change the value of the fixed $p_8 = 45 - 83 = -38$ as its final value. p_{12} also varies strongly with Q^2, but the contribution of TT is small so no further changes were made. The green lines are only to guide the eye.

Nearly final sets of parameter values for the $F_\pi - 1$ data are shown in Figs. 36, 37. The π^+ $Q^2 = 0.75$ GeV^2 parameters generally do not follow the trend given by the green line – we have looked at this carefully, and we do not see any obvious reason for this difference. A representative example of the measured experimental cross sections as a function of ϕ for a particular $-t$ bin and for low and high ϵ is shown in Fig. 38.

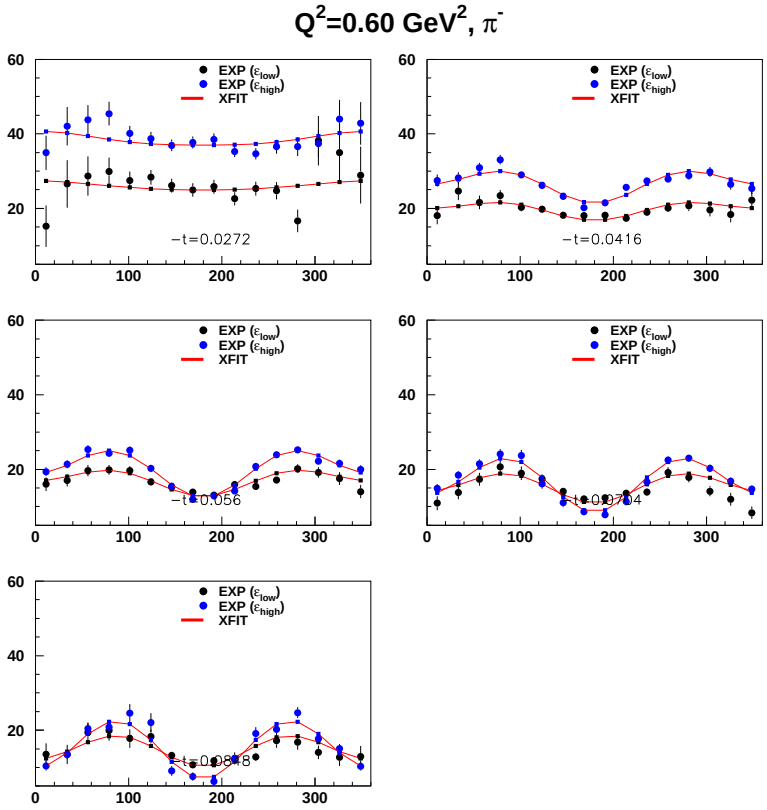

FIG. 38 Unseparated experimental π^- cross sections $\frac{d^2\sigma}{dtd\phi}$ as a function of azimuthal angle ϕ at $Q^2 = 0.60$ GeV^2 high (blue) and low (black) ϵ. The curves shown represent the fit of the measured values of the cross section to Eqn. 18. In this fit, all four parameters $\sigma_{L,T,LT,TT}$ are extracted simultaneously, separately for each $-t$ bin. As noted in Sec. III.C, separated cross sections will be published only for the lowest three $-t$ bins in this figure.

E. Systematic Uncertainties due to Missing Mass Cut and SIMC Model Dependence

The combined systematic uncertainty due to the missing mass cut and SIMC model dependence was estimated by modifying the missing mass cuts and SIMC model parameters and investigating the resulting differences on the separated cross sections in the following manner.

Missing Mass Cut Dependence:

The experimental and simulated data were analyzed with two tighter missing mass cuts, MM $<$ 0.98, 1.00. In each case, the SIMC model was iterated twice from the final parameter values obtained with the MM $<$ 1.03 cut to yield separated cross sections. A detailed comparison of the separated cross sections for each t-bin indicated that the π^- Q^2=0.6, 1.0 GeV^2 σ_L at higher $-t$ are extremely sensitive to the applied MM cut and/or the disabling of the collimator pion punch-through routine in the SIMC simulations. We believe this is a result of the incomplete ϕ coverage for these settings, as discusssed in Sec. III.C. At this late stage, we decided to exclude from publication any π^- t-bin whose σ_L changed significantly more than the statistical uncertainty

when the MM<1.03 GeV cut is replaced with MM<1.00 GeV cut in both the experimental and simulation analyses. These π^- bins were:

- Bins 4 ,5 at Q^2=0.6 GeV^2, where σ_L decreases by 46-128%.
- Bins 4 ,5 at Q^2=1.0 GeV^2, where σ_L increases by 95-305%.
- Bin 6 at Q^2=1.6 GeV^2, where σ_L decreases by 49%.

For the remaining π^+ and π^- data, the differences between the "final" separated cross sections and those determined with tigher MM cuts were computed and the standard deviation was tabulated for each $-t$ bin at each Q^2. These standard deviations for the remaining F_π-1 π^- data are in almost all cases larger than for the corresponding π^+ data, generally comparable to the statistical errors. The standard deviations are typically smallest at or near $-t_{min}$ and grow with increasing $-t$.

SIMC Model Dependence:

Separated L/T/LT/TT cross sections were obtained in six different ways and compared to the "final" cross sections.

i,ii) Separated cross sections were determined by raising and lowering σ_T in the SIMC model by $\pm$10%.

iii,iv) Separated cross sections were determined by raising and lowering σ_L in the SIMC model by $\pm(10\%+b)$, where b was taken to be approximately equal to half the value of σ_L at the highest $-t$ bin of a given kinematic setting. Due to the ϵ weighting of σ_L in the unseparated cross section, and its sharp drop off with $-t$, the effect of $\pm(10\% + b)$ is to give an approximately uniform $\pm$10% change in simulated yield. The values of b used (in units of μb/GeV^2) were:

Q^2	0.6	0.75	1.0	1.6	2.45
$b(\pi^-)$	2.0		2.0	0.5	0.1
$b(\pi^+)$	5.0	5.0	3.0	1.0	0.1

v,vi) Separated cross sections were determined by alternately setting LT=0 and TT=0 in the SIMC model. The only exception were the π^+ $F_\pi - 1$ settings, where LT=0 in the default model, so p_9 was set instead to -100.

In all cases, the other SIMC model parameters were held fixed and the model was not iterated. Unseparated cross sections were calculated using Eqn. 19 and a fit performed using Eqn. 18 to extract L/T/LT/TT. The differences between the "final" separated cross sections minus sets

i)-vi) were computed and the standard deviations tabulated for each $-t$ bin at each Q^2 in the same manner as the missing mass cut study. The model sensitivities of the L,T cross sections are generally similar to each other, and exhibit a weaker t-dependence than the MM cut sensitivities. The observed variations are about half the statistical uncertainties in these cross sections (per t-bin) of 5-10%. The sensitivities of the TT interference response functions are strongly t-dependent, being smaller for the lowest $-t$ bins at each Q^2 and increasing for the larger $-t$ bins. These higher $-t$ bins have relatively poorer statistics as well as incomplete ϕ coverage at low ϵ [as well as at high ϵ for π^- Q^2=0.6, 1.0 GeV^2]. The LT model sensitivities are smaller than for TT, and show no obvious trends.

Combined "Model-Dependence" Uncertainty:

The standard deviations each Q^2, t bin from the two above studies were combined in quadrature to obtain the combined systematic uncertainty due to the missing mass cut and SIMC model dependence (labeled henceforth as "model-dependence" for brevity). The uncertainties computed in this manner are shown as error bands, presented along with the data in the following chapter, and the values for each bin are listed as the second uncertainty in Tables XI, XII.

IV. FINAL π^-, π^+ RESULTS

A. Systematic Uncertainties

The various systematic uncertainties determined in Sec. II, III are listed in Tables IX,X. Those items not discussed explicitly in these sections are assumed to be the same as for the previously published ^{1}H analyses. These systematic uncertainties are subdivided into correlated and uncorrelated contributions. The correlated uncertainties, i.e., those that are the same for both ϵ points, such as target thickness corrections, are attributed directly to the separated cross sections. Uncorrelated uncertainties are attributed to the unseparated cross sections, with the result that in the separation of σ_L and σ_T are inflated, just as the statistical uncertainties, by the factor $1/\Delta\epsilon$ (for σ_L), which is about three. The uncorrelated uncertainties can be further subdivided into those that differ in size between ϵ points, but may influence the t-dependence at a fixed value of ϵ in a correlated way. The largest contributions to the "t-correlated" uncertainty are acceptance and kinematic offsets, and as a result, they are the dominating systematic uncertainties for, e.g. σ_L. In addition to the uncertainties listed below, are the uncertainties in the separated cross sections at each $-t$, Q^2 setting due to MM cut and SIMC model "model-dependence".

B. Separated Cross Sections

The separated cross sections are shown in Fig. 39 and are listed in Tables XI, XII. The π^+ L,T cross sections on ^{2}H are compared to our previous cross sections on ^{1}H in Fig. 40.

In the L response of Fig. 39, the pion pole is evident by the sharp rise at small $-t$. π^- and π^+ are similar, and the data at different Q^2 follow a nearly universal curve versus t, with only a weak Q^2-dependence. The T responses are flatter versus t, and with the exception of the $Q^2 = 0.6$ GeV^2 π^+ data, also follow a nearly universal curve.

Correction	Uncorrelated (pt-to-pt) [%]	ϵ uncorr. t corr. [%]	Correlated (scale) [%]
dθ_e	0.1	0.7-1.1	
dE_{beam}	0.1	0.2-0.3	
dP_e	0.1	0.1-0.3	
dθ_π	0.1	0.2-0.3	
Radiative corr		0.4	2.0
HMS β corr	0.4		
Particle ID		0.2	
Pion absorption			1.0
Pion decay	0.03		1.0
HMS Tracking (π^+)		0.4	1.0
HMS Tracking (π^-)		1.3	1.0
SOS Tracking		0.2	0.5
Charge		0.3	0.5
Target Thickness		0.3	1.0
CPU dead time		0.2	
HMS Trigger		0.1	
SOS Trigger		0.1	
Electronic DT		0.1	
HMS Cer. block. (π^-)	0.7		1.0
Acceptance	1.0	0.6	1.0
Total (π^+)	1.1	1.3-1.6	3.1
Total (π^-)	1.3	1.8-2.0	3.2

TABLE IX Systematic uncertainties for F_π-1. Those items not discussed explicitly in preceeding sections are assumed to be the same as for the published ^{1}H analysis. These are the uncertainties in: kinematic offsets, radiative corrections, pion decay, SOS tracking, trigger efficiency, CPU and electronic dead time, and acceptance. The systematic uncertainaties in each column are added quadratically to obtain the total systematic uncertainty.

Correction	Uncorrelated (pt-to-pt) [%]	ϵ uncorr. t corr. [%]	Correlated (scale) [%]
dθ_e	0.1	0.7-1.1	
dE_{beam}	0.1	0.2-0.3	
dP_e	0.1	0.1-0.3	
dθ_π	0.1	0.2-0.3	
Radiative corr		0.4	2.0
HMS β corr (π^+)	0.12		
HMS β corr (π^-)	0.18		
Particle ID		0.2	
Pion absorption			1.0
Pion decay	0.03		1.0
HMS Tracking (π^+)		0.3	0.5
HMS Tracking (π^-)		0.45	0.75
SOS Tracking		0.2	0.5
Charge		0.3	0.5
Target Thickness		0.2	0.8
CPU dead time		0.2	
HMS Trigger		0.1	
SOS Trigger		0.1	
Electronic DT		0.1	
HMS Cer. block. (π^-)	0.3		0.8
Acceptance	0.6	0.6	1.0
Total (π^+)	0.6	1.2-1.5	2.9
Total (π^-)	0.7	1.3-1.6	3.1

TABLE X Systematic uncertainties for F_π-2. Those items not discussed explicitly in preceeding sections are assumed to be the same as for the published ^{1}H analysis. These are the uncertainties in: kinematic offsets, radiative corrections, pion decay, SOS tracking, trigger efficiency, CPU and electronic dead time, and acceptance. The systematic uncertainaties in each column are added quadratically to obtain the total systematic uncertainty.

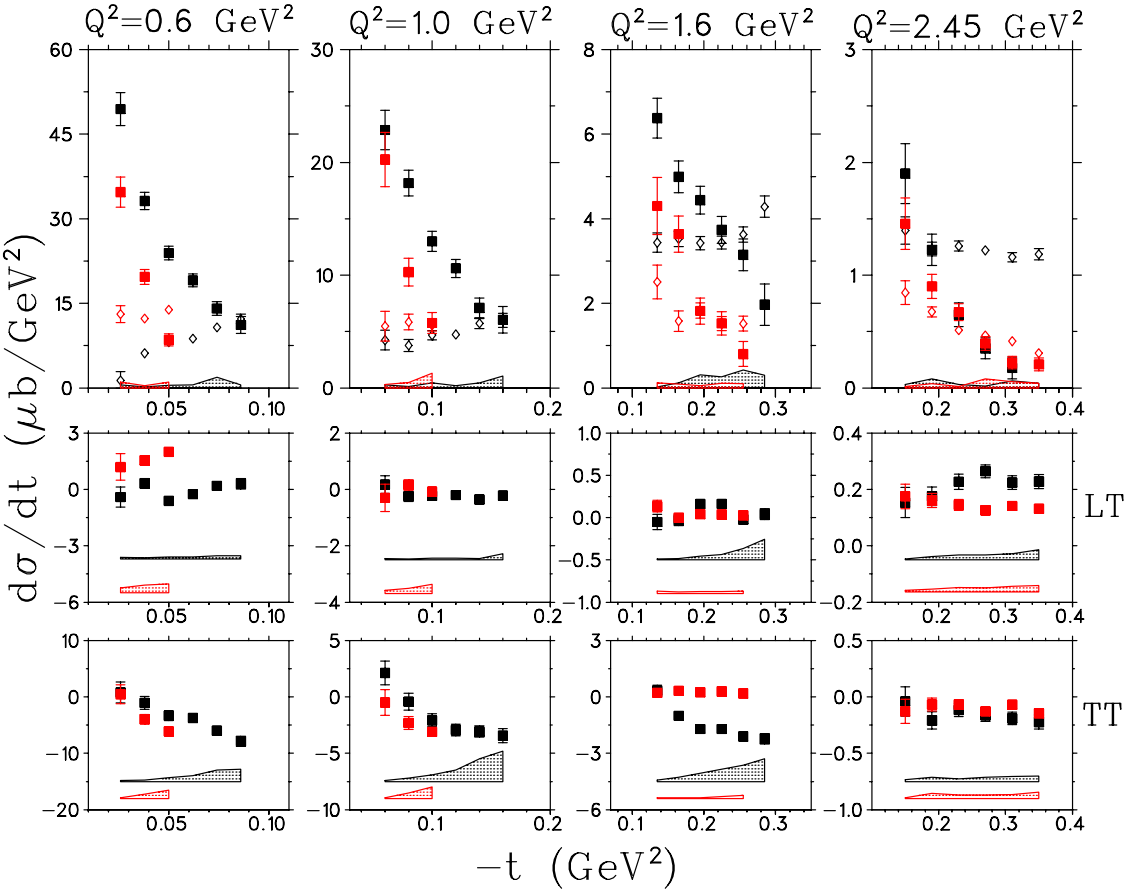

FIG. 39 Separated ^{2}H σ_L [squares], σ_T [diamonds], σ_{LT} and σ_{TT} cross sections as a function of $-t$ for the π^+ [black] and π^- [red] channels. The error bars include both statistical and uncorrelated systematic uncertainties. The "model-dependences" of the L, LT, TT cross sections are indicated by the shaded bands, by which all data points move collectively. The "model-dependences" of the T cross sections are smaller, as listed in Tables XI and XII.

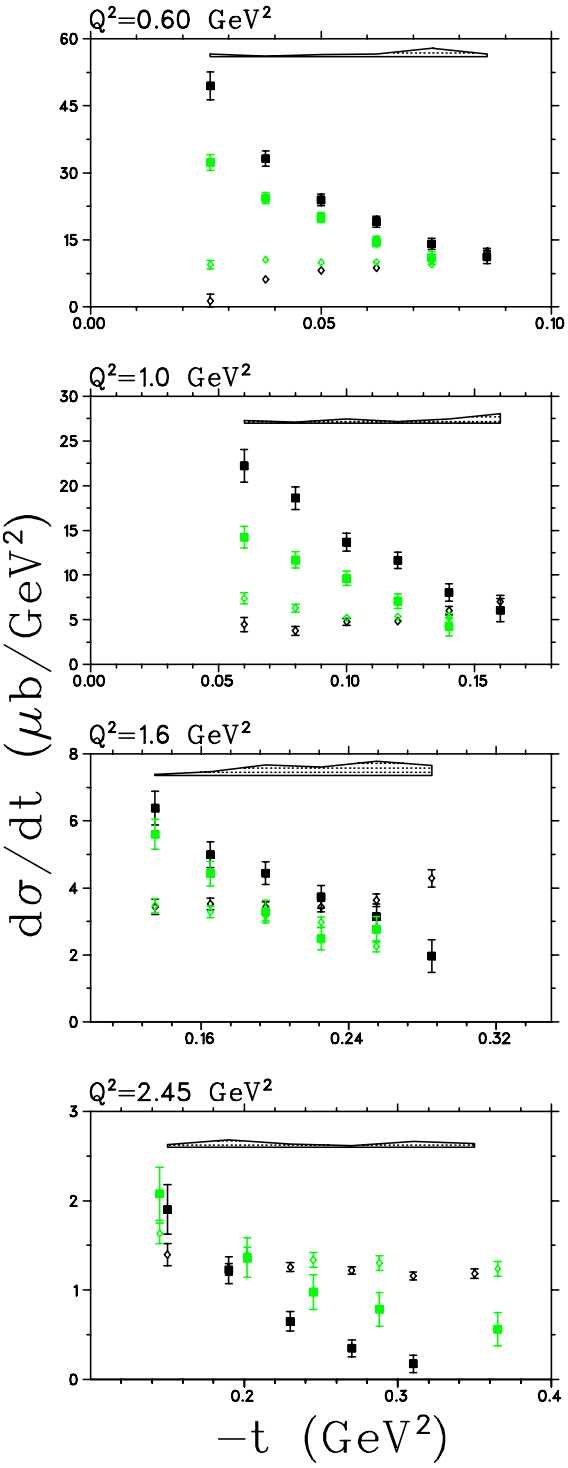

FIG. 40 Separated π^+ σ_L [squares], σ_T [diamonds] as a function of $-t$ for ^{2}H [black] and ^{1}H [green] targets. The error bars include both statistical and uncorrelated systematic uncertainties. The "model-dependences" of the L cross sections are indicated by the shaded bands, by which all data points move collectively. The ^{1}H data have not been scaled to the mean $\overline{Q^2}$, $\overline{W}$ values for each $-t$ bin of ^{2}H data. In addition, please keep in mind the issues relating to ^{2}H off-shell and other effects discussed in Sec.III.A.2 before directly comparing the ^{1}H and ^{2}H data.

$\overline{W}$ (GeV)	$\overline{Q^2}$ (GeV^2)	$-t$ (GeV^2)	σ_T (μb/GeV^2)	σ_L (μb/GeV^2)	σ_{TT} (μb/GeV^2)	σ_{LT} (μb/GeV^2)
$d(e,e'\pi^-)pp_{sp}$						
$Q^2 = 0.60$ GeV^2 $W = 1.95$ GeV						
1.9733	0.5505	0.026	13.07 ± 1.44 ± 0.69	34.74 ± 2.39 ± 1.03	0.47 ± 1.12 ± 0.12	1.12 ± 0.70 ± 0.26
1.9568	0.5765	0.038	12.31 ± 0.69 ± 0.17	19.71 ± 1.13 ± 0.36	-3.95 ± 0.48 ± 0.74	1.54 ± 0.24 ± 0.42
1.9452	0.6048	0.050	13.88 ± 0.62 ± 0.66	8.53 ± 1.03 ± 1.01	-6.13 ± 0.43 ± 1.44	2.00 ± 0.21 ± 0.48
$Q^2 = 1.00$ GeV^2 $W = 1.95$ GeV						
1.9864	0.9095	0.060	5.47 ± 1.29 ± 0.17	20.25 ± 2.25 ± 0.29	-0.50 ± 0.80 ± 0.06	-0.30 ± 0.48 ± 0.12
1.9703	0.9483	0.080	5.85 ± 0.68 ± 0.16	10.27 ± 1.16 ± 0.47	-2.31 ± 0.38 ± 0.50	0.16 ± 0.19 ± 0.19
1.9489	0.9977	0.100	5.56 ± 0.51 ± 0.46	5.75 ± 0.91 ± 1.31	-3.09 ± 0.32 ± 1.01	-0.08 ± 0.15 ± 0.33
$Q^2 = 1.60$ GeV^2 $W = 1.95$ GeV						
2.0116	1.4345	0.135	2.51 ± 0.39 ± 0.02	4.31 ± 0.66 ± 0.12	0.22 ± 0.16 ± 0.04	0.13 ± 0.07 ± 0.03
1.9867	1.5064	0.165	1.59 ± 0.24 ± 0.07	3.64 ± 0.40 ± 0.09	0.33 ± 0.10 ± 0.04	-0.00 ± 0.05 ± 0.02
1.9644	1.5650	0.195	1.83 ± 0.18 ± 0.05	1.82 ± 0.30 ± 0.05	0.25 ± 0.08 ± 0.04	0.04 ± 0.04 ± 0.03
1.9433	1.6178	0.225	1.52 ± 0.16 ± 0.09	1.53 ± 0.27 ± 0.11	0.29 ± 0.08 ± 0.09	0.04 ± 0.03 ± 0.02
1.9229	1.6664	0.255	1.52 ± 0.18 ± 0.15	0.80 ± 0.29 ± 0.10	0.19 ± 0.09 ± 0.16	0.03 ± 0.03 ± 0.03
$Q^2 = 2.45$ GeV^2 $W = 2.22$ GeV						
2.2978	2.1619	0.150	0.85 ± 0.11 ± 0.01	1.46 ± 0.22 ± 0.01	-0.13 ± 0.10 ± 0.01	0.18 ± 0.04 ± 0.01
2.2695	2.2598	0.190	0.67 ± 0.05 ± 0.01	0.90 ± 0.10 ± 0.04	-0.07 ± 0.05 ± 0.04	0.16 ± 0.03 ± 0.01
2.2400	2.3537	0.230	0.51 ± 0.03 ± 0.02	0.67 ± 0.07 ± 0.01	-0.07 ± 0.04 ± 0.03	0.15 ± 0.02 ± 0.02
2.2154	2.4289	0.270	0.47 ± 0.03 ± 0.01	0.39 ± 0.06 ± 0.08	-0.13 ± 0.04 ± 0.03	0.13 ± 0.02 ± 0.01
2.1932	2.4993	0.310	0.41 ± 0.02 ± 0.01	0.22 ± 0.06 ± 0.05	-0.07 ± 0.03 ± 0.03	0.14 ± 0.02 ± 0.02
2.1688	2.5753	0.350	0.31 ± 0.02 ± 0.03	0.21 ± 0.06 ± 0.04	-0.15 ± 0.04 ± 0.05	0.13 ± 0.02 ± 0.02

TABLE XI Separated cross sections for the $d(e,e'\pi^-)pp_{sp}$ reaction. The first errors listed are statistical uncertainties only. The second errors listed are the MM cut and SIMC model "model-dependence" uncertainties. In addition to these must be applied the systematic uncertainties listed in Tables IX and X.

$\overline{W}$ (GeV)	$\overline{Q^2}$ (GeV^2)	$-t$ (GeV^2)	σ_T (μb/GeV^2)	σ_L (μb/GeV^2)	σ_{TT} (μb/GeV^2)	σ_{LT} (μb/GeV^2)
$d(e,e'\pi^+)nn_{sp}$						
$Q^2 = 0.60$ GeV^2 $W = 1.95$ GeV						
1.9702	0.5445	0.026	1.32 ± 1.49 ± 0.10	49.44 ± 2.50 ± 0.56	0.80 ± 1.10 ± 0.21	-0.40 ± 0.53 ± 0.08
1.9572	0.5736	0.038	6.15 ± 0.64 ± 0.06	33.17 ± 1.18 ± 0.16	-1.06 ± 0.56 ± 0.24	0.32 ± 0.25 ± 0.07
1.9450	0.5953	0.050	8.15 ± 0.51 ± 0.12	23.94 ± 0.97 ± 0.47	-3.33 ± 0.46 ± 0.65	-0.61 ± 0.20 ± 0.10
1.9443	0.6092	0.062	8.76 ± 0.54 ± 0.17	19.08 ± 0.99 ± 0.54	-3.73 ± 0.49 ± 1.02	-0.25 ± 0.21 ± 0.11
1.9423	0.6146	0.074	10.73 ± 0.64 ± 0.48	14.08 ± 1.15 ± 1.90	-5.99 ± 0.61 ± 2.04	0.19 ± 0.23 ± 0.17
1.9411	0.6206	0.086	12.25 ± 0.81 ± 1.29	11.18 ± 1.45 ± 0.53	-7.74 ± 0.83 ± 2.19	0.30 ± 0.29 ± 0.18
$Q^2 = 0.75$ GeV^2 $W = 1.95$ GeV						
1.9894	0.6668	0.037	8.76 ± 1.23 ± 0.15	21.76 ± 2.03 ± 0.48	2.13 ± 0.68 ± 0.18	0.67 ± 0.29 ± 0.02
1.9691	0.6978	0.051	10.82 ± 0.80 ± 0.29	15.90 ± 1.32 ± 0.39	-0.54 ± 0.42 ± 0.38	0.42 ± 0.18 ± 0.07
1.9579	0.7259	0.065	10.34 ± 0.66 ± 0.34	14.41 ± 1.12 ± 0.28	-0.37 ± 0.37 ± 0.75	0.54 ± 0.15 ± 0.10
1.9467	0.7483	0.079	9.36 ± 0.64 ± 0.29	16.06 ± 1.08 ± 1.64	-0.69 ± 0.42 ± 1.42	0.22 ± 0.13 ± 0.11
1.9404	0.7640	0.093	9.75 ± 0.69 ± 0.37	15.82 ± 1.18 ± 4.73	-0.97 ± 0.52 ± 2.41	0.39 ± 0.14 ± 0.23
1.9357	0.7805	0.107	11.10 ± 0.81 ± 0.58	13.76 ± 1.38 ± 7.22	-1.25 ± 0.69 ± 3.45	1.12 ± 0.16 ± 0.41
$Q^2 = 1.00$ GeV^2 $W = 1.95$ GeV						
1.9970	0.8941	0.060	4.24 ± 0.82 ± 0.06	22.87 ± 1.55 ± 0.28	2.21 ± 0.71 ± 0.08	0.17 ± 0.31 ± 0.04
1.9802	0.9305	0.080	3.78 ± 0.50 ± 0.05	18.16 ± 0.95 ± 0.12	-0.42 ± 0.41 ± 0.31	-0.25 ± 0.18 ± 0.04
1.9602	0.9745	0.100	4.68 ± 0.39 ± 0.14	13.00 ± 0.76 ± 0.45	-2.07 ± 0.35 ± 0.59	-0.23 ± 0.13 ± 0.06
1.9458	1.0061	0.120	4.74 ± 0.37 ± 0.09	10.60 ± 0.72 ± 0.19	-2.93 ± 0.36 ± 1.01	-0.20 ± 0.12 ± 0.06
1.9349	1.0320	0.140	5.72 ± 0.44 ± 0.20	7.10 ± 0.83 ± 0.45	-3.07 ± 0.43 ± 2.03	-0.36 ± 0.13 ± 0.05
1.9247	1.0602	0.160	6.00 ± 0.62 ± 0.55	6.04 ± 1.14 ± 1.05	-3.44 ± 0.58 ± 2.69	-0.22 ± 0.16 ± 0.21
$Q^2 = 1.60$ GeV^2 $W = 1.95$ GeV						
2.0112	1.4353	0.135	3.43 ± 0.22 ± 0.03	6.38 ± 0.43 ± 0.03	0.34 ± 0.22 ± 0.09	-0.05 ± 0.09 ± 0.01
1.9884	1.4998	0.165	3.52 ± 0.17 ± 0.07	5.00 ± 0.34 ± 0.12	-1.01 ± 0.16 ± 0.23	-0.03 ± 0.06 ± 0.02
1.9669	1.5553	0.195	3.43 ± 0.15 ± 0.05	4.44 ± 0.30 ± 0.31	-1.70 ± 0.16 ± 0.44	0.16 ± 0.05 ± 0.05
1.9463	1.6082	0.225	3.44 ± 0.15 ± 0.11	3.74 ± 0.30 ± 0.26	-1.70 ± 0.17 ± 0.65	0.16 ± 0.05 ± 0.06
1.9276	1.6568	0.255	3.63 ± 0.18 ± 0.18	3.15 ± 0.36 ± 0.43	-2.10 ± 0.20 ± 0.86	-0.02 ± 0.05 ± 0.13
1.9097	1.7025	0.285	4.29 ± 0.25 ± 0.35	1.97 ± 0.48 ± 0.30	-2.24 ± 0.26 ± 1.20	0.04 ± 0.07 ± 0.24
$Q^2 = 2.45$ GeV^2 $W = 2.22$ GeV						
2.3017	2.1503	0.150	1.40 ± 0.12 ± 0.01	1.90 ± 0.26 ± 0.03	-0.04 ± 0.12 ± 0.02	0.15 ± 0.05 ± 0.01
2.2719	2.2518	0.190	1.23 ± 0.06 ± 0.02	1.22 ± 0.14 ± 0.08	-0.21 ± 0.07 ± 0.04	0.18 ± 0.03 ± 0.01
2.2448	2.3391	0.230	1.26 ± 0.04 ± 0.01	0.65 ± 0.11 ± 0.03	-0.12 ± 0.06 ± 0.02	0.23 ± 0.03 ± 0.02
2.2197	2.4180	0.270	1.22 ± 0.04 ± 0.03	0.35 ± 0.09 ± 0.02	-0.16 ± 0.05 ± 0.04	0.26 ± 0.02 ± 0.02
2.1977	2.4878	0.310	1.16 ± 0.04 ± 0.05	0.18 ± 0.10 ± 0.06	-0.19 ± 0.05 ± 0.05	0.22 ± 0.02 ± 0.02
2.1750	2.5570	0.350	1.19 ± 0.05 ± 0.04	-0.10 ± 0.11 ± 0.04	-0.22 ± 0.06 ± 0.05	0.23 ± 0.02 ± 0.04

TABLE XII Separated cross sections for the $d(e,e'\pi^+)nn_{sp}$ reaction. The first errors listed are statistical uncertainties only. The second errors listed are the MM cut and SIMC model "model-dependence" uncertainties. In addition to these must be applied the systematic uncertainties listed in Tables IX and X.

C. π^-/π^+ Separated Response Function Ratios

Separated cross section π^-/π^+ ratios are shown in Fig. 41 for σ_L and σ_T. L/T Ratios for the π^+ and π^- reactions are shown in Fig. 42.

Fig. 41 shows the first determination of R_L above the resonance region. The ratio is approximately 0.8 near $-t_{min}$ at each Q^2 setting, as predicted in the large N_c limit calculation of Ref. (17). The data are generally lower than the predictions of the pion-pole dominated models of Ref. (15; 18; 19). A simple estimate, under the not necessarily realistic assumption that the isoscalar and isovector amplitudes are real, is that $R_L = 0.8$ is consistent with $|A_S/A_V| = 6\%$. These results indicate that pion exchange dominates the forward longitudinal response even $\sim 10\ m_\pi^2$ away from the pion pole. This is relevant for the extraction of the pion form factor from electroproduction data, which uses a model including some isoscalar background.

Also in Fig. 41 are the first $R_T \equiv \sigma_T^{\pi^-}/\sigma_T^{\pi^+}$ results in electroproduction at high momentum transfers. The behavior of R_T changes dramatically with increasing Q^2 over a fairly small range in $-t$, reaching 0.23-0.27 at larger Q^2 and $-t$. It is interesting to note that this value is reached at a much lower value of $-t$ than for the unseparated ratios of Ref. (3). A value of $-t = 0.3$ GeV^2 seems quite a low value for quark charge scaling arguments to apply directly. This might indicate the partial cancellation of soft QCD corrections in the formation of the π^-/π^+ ratio. The models of Refs. (15; 18; 19) do not accurately predict R_T at $-t_{min}$, although (19) does much better at higher $-t$. The Goloskokov-Kroll GPD-based model does much better at R_T, but parameters in this model are optimized for small skewness ($\xi < 0.1$) and large $W > 4$ GeV. The application of this model to the kinematics of our data requires a substantial extrapolation in W and ξ, and so one should be cautious in this comparison. Indeed, although the model does a reasonable job at predicting the π^-/π^+ ratios, the agreement of the model with our σ_T is not good (20). Further theoretical work is clearly needed to investigate alternate explanations of the observed ratios.

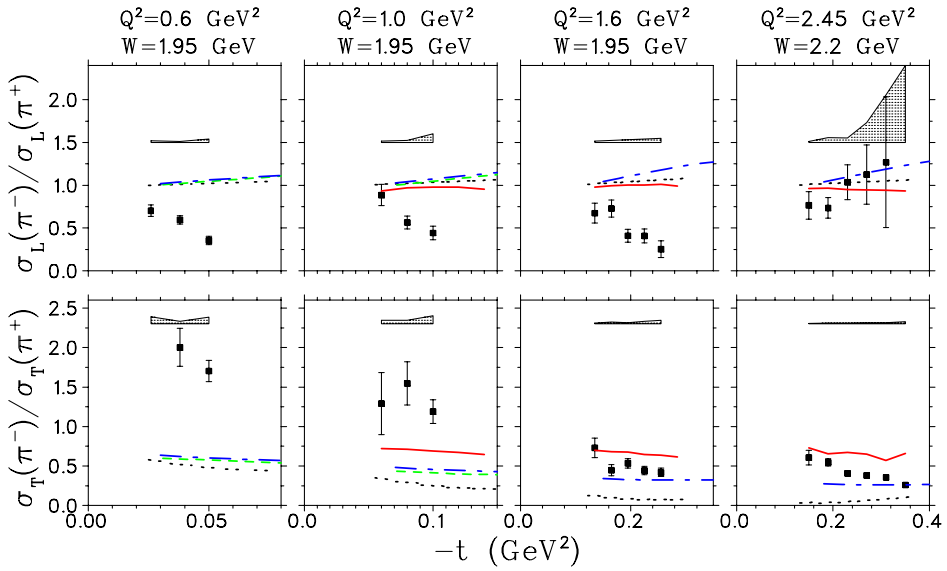

FIG. 41 π^-/π^+ separated cross section ratios as a function of $-t$ for σ_L and σ_T. The error bars include statistical and uncorrelated systematic uncertainties. The model-dependences of the ratios are indicated by the shaded bands, by which all data points move collectively. The dotted black curves are predictions of the VGL Regge model (15) using the values $\Lambda_\pi^2 = 0.405, 0.503, 0.654, 0.636$ GeV^2, as determined from fits to our ^{1}H data (4), and the solid red curves are predictions by Goloskokov and Kroll (20), both models calculated at the same $\overline{W}$, $\overline{Q^2}$ as the data. The dashed green curves are predictions by Kaskulov and Mosel (18), and the dot-dashed blue curves are the predictions by Vrancx and Ryckebusch (19), both models calculated at the nominal kinematics.

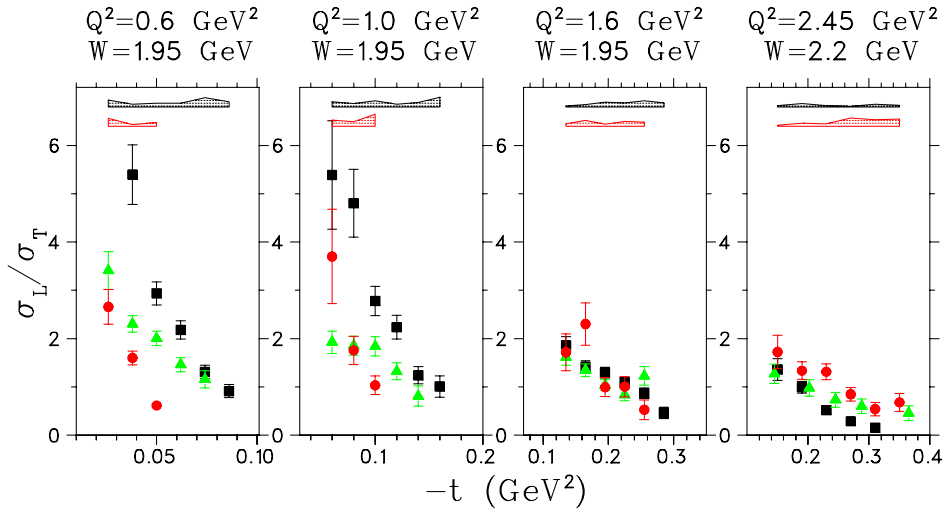

FIG. 42 L/T separated cross section ratios as a function of $-t$ for π^+ [black squares] and π^- [red circles] production on ^{2}H, and for π^+ on ^{1}H [green triangles]. The model-dependences of the ratios are indicated by the shaded bands, by which all data points move collectively.

References

[1] F. A. Berends, Phys. Rev. D **1**, 2590 (1970).
[2] F. Gutbrod and G. Kramer, Nucl. Phys. **B49**, 461 (1972).
[3] P. Brauel*et al.*, Z. Phys. **C3**, 101 (1979).
[4] H.P. Blok *et al.*, Phys. Rev. C **78**, 045202 (2008).
[5] V. Tvaskis, Ph. D. thesis, Vrjie Universiteit te Amsterdam (2004).
[6] J. Volmer, *The Pion Charge Form Factor via Pion Electroproduction on the Proton*, Ph.D. Thesis, Vrije Universiteit Amsterdam (2000).
[7] Chuncheng Xu, "Optics Check for different Psos", `http://lichen.phys.uregina.ca/ fpiweb/xu/OPTCHECK.html`.
[8] T. Horn, Ph D. thesis, University of Maryland (2006).
[9] D. Gaskell, *Longitudinal Electroproduction of Charged Pions on Hydrogen, Deuterium, and Helium-3*, Ph.D. Thesis, Oregon State University (2001).
[10] "Atomic and Nuclear Properties of Materials", Particle Data Booklet (2009).
[11] D. M. Koltenuk, Ph.D. thesis, University of Pennsylvania (1999).
[12] F. James, MINUIT - *Function Minimization and Error Analysis for Physical Sciences*, Reference Manual (1993).
[13] P. Brauel *et al.*, Phys. Lett. **B69**, 253 (1977).
[14] C. J. Bebek *et al.*, Phys. Rev. D **17**, 1693 (1978).
[15] M. Vanderhaeghen, M. Guidal, J.-M. Laget, Phys. Rev. C **57** 1454 (1998).
[16] G.M. Huber *et al.*, Phys. Rev. C **78**, 045203 (2008).
[17] L.L. Frankfurt, M.V. Polyakov, M. Strikman, M. Vanderhaeghen, Phys. Rev. Lett. **84** 2589 (2000).
[18] M.M. Kaskulov, U. Mosel, Phys. Rev. C **81** 045202 (2010).
[19] T. Vrancx, J. Ryckebusch, arXiv:1310.7715.
[20] S.V. Goloskokov, P. Kroll, Eur. Phys. J. C **65** 137 (2010); Eur. Phys. J. A **47** 112 (2011); and Private Comminication 2013.